Development of Hybrid Fibrin Collagen – Single Walled Carbon Nanotube Hydrogels for Cardiac Tissue Engineering

A thesis submitted by:

Jeffrey Neale

In partial fulfillment of the requirements for the degree of

Master of Science in Biomedical Engineering

Tufts University

Advisor: Dr. Brian Timko

ABSTRACT

The heart is known for being one of the least regenerative organs in the human body. Once damaged, there is no treatment or therapy that can restore initial function. The umbrella that encompasses cardiovascular diseases account for 32% of deaths worldwide according to the World Health Organization making it the world’s most significant health burden, and what some consider to be the next great pandemic. Tissue engineering seeks to solve this problem by developing biomaterials able to mimic native myocardial tissue to promote cardiomyocyte growth and development that can restore natural function.

The aim of this work is to engineer a three-dimensional hydrogel made from natural biopolymers fibrin and collagen, that can incorporate electrically conductive carbon nanotubes (CNTs). Natural biopolymers fibrin and collagen are clinically relevant biomaterials, that when combined, offer biological activity of both proteins as well as enhanced mechanical properties. The addition of carbon nanotubes significantly improves mechanical strength while addressing a key limitation of natural biopolymers, their lack of electrical conductivity.

Herin, we present the successful dispersion of single-walled carbon nanotubes into fibrin-collagen hydrogels and demonstrate that increasing nanotube concentrations enhance the elastic and compressive properties of the material, while also supporting the culture of neonatal rat cardiomyocytes.

ACKNOWLEDGEMENTS

To Dr. Brian Timko, thank you for years of guidance and support. It has been a privilege to learn from you as I make this embark into a new career and chapter in my life. I cannot express how grateful I am for the opportunity you gave me.

To Dr. Mark Cronin-Golomb, thank you for welcoming me to the Tufts community and guiding me into the biomedical engineering program. I wouldn’t have been able to make the transition into this program without you.

To Laura Place, for all the trainings and assistance offered over the years, your help made all the difference.

To Olurotimi Bolonduro, for showing me the ropes in the lab, and always being around to answer questions and offer help.

TABLE OF CONTENTS

List of Tables

List of Figures

1. Introduction

In the late 20th century, cardiovascular diseases (CVD) surpassed infectious diseases as the leading cause of death worldwide [1]. For the past thirty years it has remained, and to date is annually responsible for 32% of deaths [1]. Among the range of diseases under the CVD umbrella, ischemic heart disease is considered the most prevalent, accounting for 12% of deaths worldwide. In the United States, annual data published by the American Heart Association, National Institutes of Health, and other government agencies show dying from heart disease, stroke, and coronary heart disease has been dropping. However, despite this, heart failure has remained the leading cause of death since 1921 [1,2].

The heart muscle is the center of the circulatory system. A pump with the sole purpose of moving blood throughout the body by creating high hydrostatic pressure pumping blood out, and low pressure to bring it back in. While visually simplistic, clockwork like precision and regulation are required, governed by a complex interconnection of electrically and mechanically coupled contractile cells, called cardiomyocytes (CMs). During an ischemic event such as myocardial infarction (MI), a blockage of the coronary artery rapidly leads to tissue necrosis [6]. Here time is a major factor as anti-fibrinolytic agents or primary percutaneous coronary intervention (PCI) must be used to re-establish blood flow to limit tissue damage [6]. However, after damage occurs, the results are irreversible as the adult mammalian heart is one of the least regenerative organs [5]. Without the ability to regenerate CMs, cardiac fibrosis fills the damaged tissue to restore structural integrity using fibrous proteins [7]. While there are several different types of scarring that can occur, the resulting dysfunctions from a stiffened myocardial matrix and impaired electrical conductance commonly led to heart failure and death [7].

Standard care for these patients has improved vastly over the years, from pharmacotherapy and surgical interventions, however, there still is nothing that can be done to prevent heart failure [9]. The last resort for these patients is still cardiac transplantation but with a constant shortage of donors few are that lucky [9]. Even if a patent is fortunate enough to get a new heart, they will be on a lifetime of immunosuppressants. The task of cardiac regeneration is monuments and currently there are three promising areas being explored with significant advances over the past several decades [9]. To effectively describe the approaches to cardiac repair, it is first essential to establish a basic understanding of cardiac physiology and structure.

1.1 Cardiac Physiology

The heart is hollow, vaguely cone shaped, and weighs roughly 250-350 grams. It is positioned in the center of the thoracic cavity between the lungs, encompassed by a double walled sac called the pericardium [12]. The outer layer, or fibrous pericardium, is made up of dense connective tissue anchoring it to the surrounding structures, while the inner visceral pericardium serves as part of the heart wall [12]. The two layers are separated by a layer of thick fluid, or pericardial fluid, that acts as a natural lubricant, reducing friction as the heart beats [12]. The heart wall is made of three layers; the outer epicardium, the myocardium; containing the muscle tissue, and the inner endocardium consisting of a thin layer of squamous epithelial tissue [12].

The muscle itself is divided laterally into two sides and is separated by a thick partition called the septum. This division creates the four chambers with two superior thin-walled atria and two inferior thick-walled ventricles, responsible for producing areas of low and high pressures respectively [12]. Each chamber has a corresponding valve, allowing blood to flow in one direction and not the other. The opening and closing of valves in response to pressure changes caused by the contraction and relaxation of the ventricles is referred to as the cardiac cycle.

At the beginning both atria and ventricles are relaxed, referred to as diastole. Blood flows from the inferior and superior venae cavae into the right atrium, and from the four pulmonary veins into the left atrium. As they fill pressure rises and when triggered, the atria contract, the pressure rises further causing the atrioventricular valves to open and blood to fill the ventricles. The contraction of the atria (atrial systole) then follows depolarization represented by the P wave of an ECT as seen in [Figure 1.] [11]. Ventricular systole follows the depolarization of the ventricles and is represented by the QRS complex [Figure 1.] and is described as having two phases. First, as contraction begins, pressure within the chamber rises. While it's not enough to open the semilunar valves, it moves blood back towards the atria, closing the tricuspid and mitral valve [11]. This early phase is known as isovolumic contraction. Second is the ventricular ejection phase, where the contraction of the ventricle generates enough pressure to open the pulmonary and aortic semilunar valves. While the pressure created is much higher in the left ventricle, both move the same volume of blood [11]. Ventricular diastole, also defined by two phases, follows repolarization of the ventricles, and is shown by the T wave of the ECG [11]. First, the ventricular muscle relaxes, pressure begins to fall until its lower than that of the pulmonary trunk and aorta. At that point blood flows back into the heart and the semilunar valves close preventing backflow. In this early phase of ventricular diastole there is no change in the volume of blood within the ventricles and thusly termed, isovolumic ventricular relaxation phase [11]. In late ventricular diastole, as the muscle relax the pressure drops below that of the atria. This causes the tricuspid and mitral valves to open and blood flows into the ventricles completing the cycle [11].

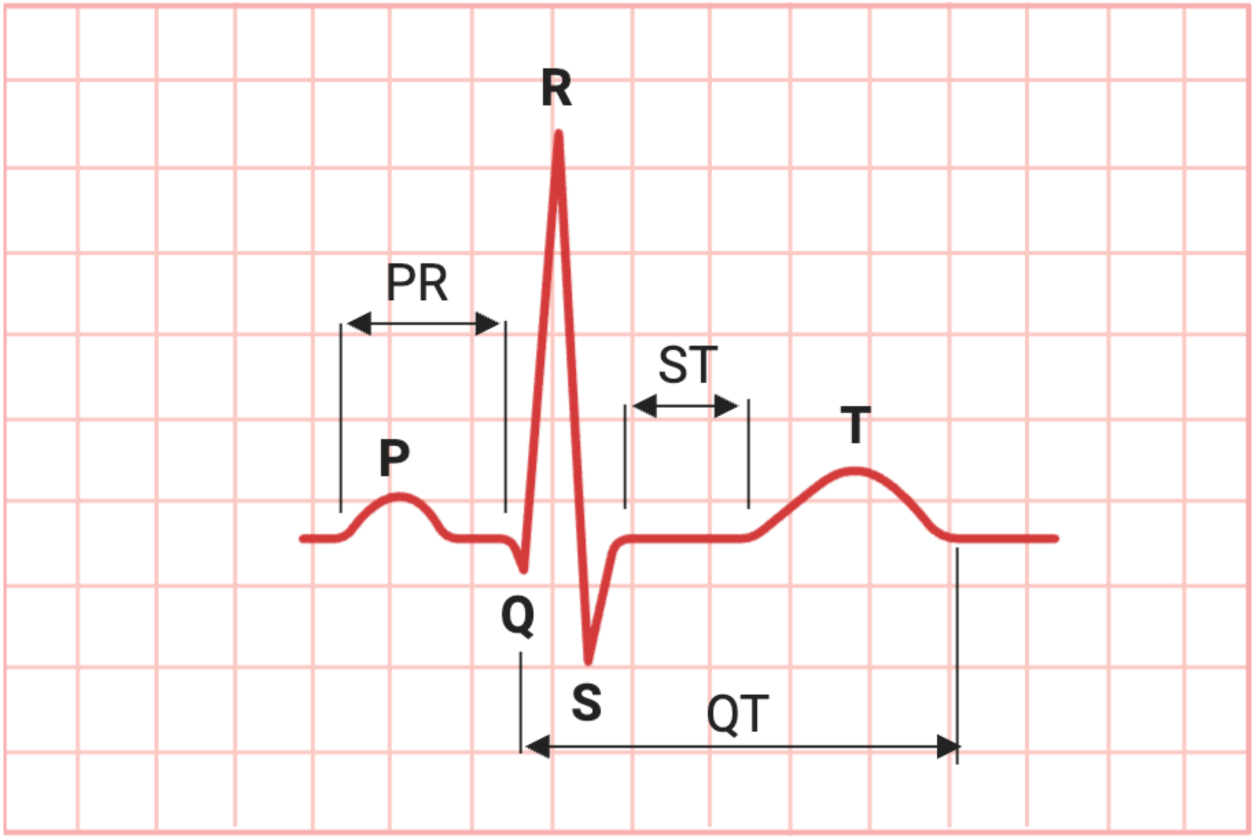

FIGURE 1 PQRST WAVE. IMAGE CREATED IN BIORENDER. (BIORENDER, 2025)

This circulation of blood throughout the body is mechanistically defined as cardiac output (CO) [11]. The volume of blood the heart pumps per minute, is equal to heart rate (number of beats per minute) multiplied by stroke volume (SV), the amount of blood pumped from the left ventricle each beat [11]. Heart rate can vary, with the body moving ~5-6 L/min at rest, and up to 35L/min during high intensity exercise [11]. This ability of the heart to adapt to these changes is known as the Frank-Starling mechanism. The response can be described simply as the more the heart is stretched, i.e larger volume of blood, the greater the subsequent force of ventricular contraction will be [11].

This coordinated contraction is a result of how the heart's advanced electrical system stimulates these cells. Electrical signals propagate along surface membranes with contractions that follow, because unlike skeletal muscle, cardiac muscle cells are both physically and electrically connected [12]. The myocardium is the contractile layer of the heart, made up of specialized muscle cells called cardiomyocytes. These cells are branched, interconnected, and separated the network of connective tissue and capillaries known as the endomysium [12]. They typically contain one to two nuclei, and mitochondria that make up to 25-35% of each cell, preventing the cells from fatiguing [12]. These cells muscle cells are unique as they operate via autorhythmicity.

Within the right atrium are a group of specialized myocytes called pacemaker cells [12]. These cells constitute the beginning of the cardiac conduction system and is known as the sinoatrial node (SA node) [12]. They are characteristically unique, have no true resting potential but rather generate consistent action potentials by undergoing spontaneous depolarization keeping the heart beating at the correct rhythm [12]. This property is caused by "leaky" ion channels. Below

40mV, Na^{2+} ions begin to flow into the cell. The membrane potential drops to -60mV as Na^{2+} continues to flow in, raising it to the -40mV threshold, where Ca^{2+} channels open further depolarizing the cell and causing the action potential to fire [12]. At the peak of depolarization, calcium channels inactivate, K+ ions leave the cell, and the voltage returns to -60mV and membrane potential is restored due to several ionic pumps, restarting the cycle. When changes occur and the signal from the SA node is disrupted or fails, the other pacemaker cells can take over causing changes to the heartbeat which can lead to an artificial pacemaker being implanted [13].

The electrical signal that is generated propagates from the SA node through myocytes with a different ion channel, and calcium handling ability. The typical cardiomyocyte (non-pacemaker) has a resting membrane potential of -90mV, created by the concentration difference in key ions, K+, Na+. Ca^{2+}, and Cl-, in and out of the cell [13]. The Nernst Equation describes the equilibrium potentials for each ion given their intra and inter cellular concentration. The classic cardiac AP is divided into 5 distinct phases and are associated with changes in membrane permeability to the previously mentioned ions. Their movement is controlled by such permeability and thus changes the membrane voltage (Vm). Briefly: Phase 0 constitutes the fast depolarization of the cell causing rapid increase in Na+ conductivity through the opening of Nav1.The AP amplitude is determined by extracellular Na+ where it moves from roughly 140 mEq/L to ~20mEq/L, moving the membrane potential from -90mV to -65mV, where it can no longer be excited [13].Once this threshold is reached, fast acting sodium channels open bringing the membrane potential rapidly to +30mV. Phase 1, is a period of brief repolarization where chemical and electrostatic forces favor the expulsion of K+, leading to phase 2. Known as the plateau phase, there is a net influx of Ca^{2+} that is however balanced by continued efflux of K+. Phase 3 brings the final repolarization when the K+ leaving the cell starts to exceed the amount of Ca^{2+} leaving the cell. This ends in phase 4 where the cell is sitting at its resting membrane potential [13].

The cardiac conduction system moves these electrical signals from the SA to the atrioventricular (AV) node on the other side of the right atrium. This node delays the signal, allowing the atria to finish contracting, filling the ventricles. Ventricles are so large they need an evenly distributed electrical to coordinate the contraction, and do so from the bottom up, accelerating the blood out into the large diameter arteries [12,13]. To accomplish this, the electrical signal travels from the AV node down to the inferior end of the heart via the atrioventricular bundle (bundle of His), then branching out to the left and right ventricle, and finally to Purkinje fibers completing depolarization in all neighboring cells completing the ventricular contraction [12,13].

1.2 Cardiomyocyte Structure & Function

The highly organized structure of the cardiac muscle cell is key to discussions about its electrical and mechanical properties, where form truly follows function. Therefore, it is important to identify, for future reference, the specialized structures of responsible for transforming a single action potential into a contraction and relaxation of the full heartbeat.

Cardiomyocytes are highly specialized cells designed to generate force. Smaller than skeletal muscle cells, they are roughly 10 μm in diameter and 100 μm in length [14]. These muscle cells or muscle fibers contain myofibrils bundled inside which are made up of thousands of repeating contractile units known as sarcomeres. They are classified as a type of striated muscle, are mononucleated (typically) and have an extremely high density of mitochondria [14]. The first major cellular component is the cell membrane, the sarcolemma. A lipid bilayer forming a coalescence of the basement membrane and plasma membrane, the sarcolemma enfolds the myocyte and features integrin binding sites connecting the myocyte to the ECM [15,16]. In cardiomyocytes, the action potentials last from 150 to 300 msec, significantly longer than skeletal muscle, which is due to the slow influx of Ca^{2+} through voltage-gated L-type calcium channels in the sarcolemma [14]. The amount of Ca^{2+} the AP triggers to enter muscle cell is small, serving as a signal to trigger the release of Ca^{2+} from the pool that contained in the sarcoplasmic reticulum (SR). In cardiac physiology this is known as calcium-induced calcium release [15,16]. Once inside the cell, Ca^{2+} binds to ryanodine receptors (RYRs) on the terminal end of the SR. RYRs are Ca^{2+} gated calcium channels and released a greater amount of Ca^{2+} into the cytosol, facilitating excitation – coupling, or electrochemical coupling in cardiac cells, resulting in contraction [14]. The relaxation of the cell is more complex than that of skeletal muscle. Ca^{2+} must be pumped back into the SR via SERCA (SR Ca^{2+} -ATPase) as with the skeletal system. However, in additional, trigger calcium must be forced out of the sarcolemma by sarcolemic Ca^{2+} - ATPase and by 3Na+-1Ca^{2+} antiporter (3 Na+ ions enter the cell for each Ca^{2+} ion moved out) preventing the SR from continuously expelling Ca^{2+} [14]. This expulsion of Ca^{2+} competes with the intake of Ca^{2+} in the SR by SERCA and thus reduces the accumulation of free calcium in the cytoplasm.

In addition to the sarcolemma's roll in calcium handling, it has been proposed that integrin interactions with the extracellular and intracellular spaces are a fundamental aspect of force transduction in myocyte shortening and ventricular contraction [16]. The structure of the sarcolemma is also responsible for the next defining feature of the cardiomyocyte, the intercalated disc. A specialized junction forming the chemical and mechanical linkages between each cell.

Intercalated discs are made up of three distinct complexes and are responsible for maintaining structure, transmit mechanical power, and propagate electrical signals. Adherens junctions (AJs) or fascia adherens, couple and transmit power from one cell to another contributing to the overall tissue structure and function of the heart. These protein structures contain two basic units, cadherin/catenin and nectin/afadin complexes, that link the cellular membrane and cytoskeletal components at specific contact points in the intercalated disc [17]. The cadherin/catenin complex are type 1, single-pass transmembrane glycoproteins that mediate calcium dependent intracellular adhesion [17]. Providing one of the key attributes of cardiac tissue, desmosomes are intercellular junctions that mechanically integrate adjacent cells. The importance of these junctions is highlighted by their location within the tissue where they are consistently subjected to strong physical forces and are required to resist mechanical stress and prevent detachment under normal contractile conditions [17,18]. Within the cell, bundles of intermediate extend out towards the plasma membrane e where they attach to transmembrane proteins desmoglein-2 and desmocollin-2 via cytoplasmic plaque and intermediate adhesive complexes [17,18]. Electrical signaling and continuity is provided by gap junctions. These microdomains are made up of connexin 43 proteins, creating low resistant channels that allow the flow of ions from one cell to another generating electrical signal propagation. The channels themselves are composed of two opposed hexamers of connexin proteins forming a cylindrical pore [18].

As mentioned, sarcomeres are responsible for the cell's contraction and relaxation. These repeating units run the length of the cell and give cardiac muscle its striated appearance and its functional linear pumping action [14]. The contractile units, actin and tropomyosin, and the troponin complex respond to previously mentioned increase in extracellular Ca^{2+}. The contraction of the sarcomere can be thought of in terms of bringing its two vertical ends, referred to as Z-disc or Z-lines, towards the center (M-band) by the contractile filaments' actin and myosin. Designated the "I" band, thin actin strands intersect either side of the Z-disc and interact with thick myosin strands. Contraction via the cross-bridge system is electrically activated upon the increase of intracellular $Ca^{2\ +}$, or calcium induced calcium release [14]. It has been proposed that myofilaments operate in terms of three different states of biochemical equilibrium transitions that reflect the interactions between sliding filaments [14]. Blocked, or B-state, Ca^{2+} is not bound to cardiac troponin C (cTnC) and the myosin-binding sites on actin are sterically blocked by tropomyosin (14). Closed, or C-state, when Ca^{2+} binds to cTnC, exposing the myosin binding sites on actin by causing the troponin complex to move roughly 25 degrees (14). Finally, the open or M-state, where tension is generated by the formation of cross-bridges and force is generated. When action potential reaches the cell, a rapid increase in intracellular Ca^{2+} occurs causing transition from one state to the next, resulting in a contraction and the shortening of the sarcomere and ultimately the cell [14].

Microtubules make up the group of proteins that gives these cells mechanical stability, elasticity, spatial organization, and long-range communication capacity are referred to as the sarcomeric cytoskeleton [19,20,21]. As with all mammalian cells, cardiomyocytes rely on the three cytoskeletal polymers, actin, intermediate filaments, and microtubules, to define their shape and structure [19]. However, changes in cardiomyocytes filament organization dramatically affect the stiffness characteristics that are exhibited. To this point, microtubules, made of a- and b-tubulin that assemble into protofilaments that make hollow polymer with a diameter of 25um, do not determine the cells overall stiffness despite being the stiffest constituent. To resist deformation and withstand contractile forces, rod-like filaments are crosslinked, giving the ability to respond dynamically. This crosslinking gives rise to two fundamental cytoskeletal properties, non-linear stiffing and viscosity [20,21]. As cells contract and strain increases, the crosslinked filaments transition from compact and coiled to aligned. During contraction, microtubules buckle to match the shortening of the sarcomere, by way of their crosslinking to desmin intermediate filaments at the sarcomere Z-disc. The amount of force they can withstand and range they can stretch without breaking is determined by the density of crosslinking [20,21].

1.3 Pathophysiology of Myocardial Infarction

The heart, the brain, and the lungs, are the three vital organs that cannot fail, or the dying process begins [23]. The heart being at the center, supplying the metabolic necessities for every organ. For the purposes of this work, myocardial infarction will be used as the pathological example to demonstrate how damage occurs and the consequences thereof.

When there is an occlusion of the coronary artery, the sudden reduction in metabolites causes detrimental changes within 15-20 seconds. Cardiomyocytes are dependent on a large and steady supply of ATP to support cellular function which is largely derived from oxidative phosphorylation (aerobic) and glycolysis (anaerobic) [24,25]. With mitochondria accounting for a third of the cardiomyocytes volume, over 95% of ATP is generated by oxidative phosphorylation [24,25]. An astounding 60-70% of that ATP is used to generate contraction consumed at a rate of ~0.5 umol/g wet wt/s [24]. The high energy phosphate supply in the heart is small and depleted within only a few seconds, demonstrating how quickly impaired oxygen delivery can cause cardiac dysfunction. Within minutes the lack of ATP causes reduction in contraction and after 40-60 minutes is nearly depleted. Clinically referred to as “the point of no return”, this is where irreversible structural damage is done [25].

The time at which patients receive medical attention determines the amount of damage that is done, however the point at which they receive intervention does not stop the clock on the damage being done. Ischemia-reperfusion injury (IRI) is the paradoxical treatment following MI. Traditionally the sooner blood flow can be restored the lower the risk of tissue damage and mortality [26]. However, there is a period after the supply of blood returns where it causes imbalances that further damage the myocardium. Because the molecular mechanisms that occur in the two phases are different, these injuries must be looked at in terms of both phases separately and are termed ischemia/reperfusion injuries [26-30]. While the mechanism for ischemia/reperfusion injuries has not yet been elucidated, the mechanisms that are known can give a detailed picture.

Ischemia begins when the blood supply decreases to the point where the metabolic demands of the cell are no longer being met. The change from aerobic to anaerobic metabolism not only produces less ATP, but lactic acid, decreasing the pH within the tissue, further hindering ATP production [27]. That ATP is broken down to ADP, AMP and inosine monophosphate (IMP), and finally into adenosine, inosine, hypoxanthine and xanthine [27].

At the cellular level, the drop in ATP causes ATP-dependent ionic pumps, Na+/K+/Ca^{2+}, to fail, resulting in the loss of previously mentioned ionic gradients [28]. Cytosolic Na+ rises, drawing in water attempting to correct the imbalance, while potassium is expelled into the interstitium [28]. Mitochondria release calcium into the cytoplasm and extracellular space activating a mitochondrial calcium-dependent cytosolic protease converting xanthine dehydrogenase into xanthine oxidase. The breakdown of lipid membranes begins to break down due to phospholipases, increasing fatty acid circulation [28].

While reperfusion is required to stop further damage to the myocardium, it can also lead to reperfusion arrhythmia, myocardial stunning, and cardiomyocyte death due to oxidative stress, inflammatory response, calcium overload, and mitochondrial dysfunction [29]. During reperfusion, the substrates for ATP production and oxygen are reintroduced, pH normalizes, and waste products are flushed from the injury [29,30]. Once blood flow is reestablished, the electron transport chain becomes active generating reactive oxygen species [29,30]. Oxidative stress (OS) refers to the imbalance of oxidants and antioxidants within the cardiomyocyte and is considered the main contributor to pathophysiological damage following infarction. Caused by reactive oxygen species (ROS), is the main contributor to pathophysiological damage following infarction [30]. OS refers to the imbalance of ROS such as hydrogen peroxide, superoxide, singlet oxygen, etc [31]. At normal physiological levels they function as signaling molecules. High levels of ROS lead to structural and functional damage of DNA and proteins [31].

From ischemia, to reperfusion, to homeostasis, oxidative stress, apoptosis, and inflammation are the major mechanisms contributing to cardiomyocyte loss [30,31]. Autophagy, or the breakdown of unnecessary cellular components by lysosomes, has been identified as a crucial component as the accumulation of cellular debris, particularly proteotoxicity [29].

Reperfusion causes the rapid normalization of extracellular pH, forming a strong H+ gradient across the plasma membrane [31]. This gradient causes a massive flow of Na+ inside the cells, trying to equilibrate the excess H+ ions through the Na+/H+ exchanger [31]. The forces in the sodium-calcium or NCX exchanger to secret Na+ outside the cell to balance its accumulation and importing Ca^{2+}. It takes about 30-60 min to reestablish physiological calcium levels, however the excess in transient Ca^{2+} accumulation in the cytoplasm triggers calcium-dependent lipases and proteases and trigger cell hyper-contraction and mitochondrial permeability transition pore (mPTP) opening [32]. Prolonged or higher conductance opening leads to harmful effects, including mitochondrial depolarization, swelling, and massive release of cytochrome C and Ca^{2+}, which trigger the intrinsic apoptotic pathway and necrosis respectively. The loss of structural tissue makes the area susceptible to deformation, thinning of the infarct region and dilation of the cavity occur because of necrotic tissue [32].

This loss of functional myocardium leads to cardiac dysfunction. The term, ‘remodeling’, is used clinically to describe the body’s process of replacing necrosed tissue with fibrous scar tissue, progressively impairing contractile functions eventually heading to heart failure. Infarctions cause millions of myocytes to die simultaneously, a large cellular response is initiated driven by cell-cell signaling. Necrosed cardiomyocytes release complement, danger-associated molecular patterns (DAMPs), and other signaling molecules that release complement and other molecules that initiate the inflammatory response recruiting macrophages, lymphocytes, and neutrophils to the site [31]. This inflammatory stage results in the ECM being degraded and dead cells phagocytosed. While the degradation effects of neutrophils are damaging, they are necessary for creating space for scar formation [31,32]. Macrophages and neutrophils degrade the extracellular collagen matrix, angiogenesis begins, and fibroblast-like cells are recruited and begin to replicate [32]. The remodeling process is usually completed in 6-8 weeks following the event resulting in a fibrillary scar of cross-linked collagen capable of withstanding deformation [32]. If the damage is large enough, the entire heart will be involved in this process and fibrous tissue will start to appear throughout the heart remodeling healthy tissue [32].

2. Cardiac Tissue Engineering

The current landscape of cardiac rehabilitation and medical intervention for CVD are a slew of medications and surgical procedures. Preventative and treatment medications are an early line of defense. Nitroglycerine for fast relief of angina by relaxing blood vessels and decreasing the amount of work required of the heart [33], beta blockers for influencing chemical signaling and changing heart rate, calcium channel blockers as antihypertensive agents [33]. Procedures and surgeries are used to restore blood flow and normal heart rhythm. Angioplasty can restore blood flow when plaque has built up inside the arterial wall by inflating a small balloon. Alongside, stents can be used to keep the space open. Coronary artery bypass surgery is used to restore blood flow to areas of the heart where it’s necessary by using blood vessels from other parts of the body to create a way around the blockage. As the condition becomes more severe, surgeries become more invasive for example pacemaker and defibrillator implantation, ventricular assist device implantation and valve repair/replacement surgeries. Surgical complications can lead to infection, bleeding, kidney failure, stroke, heart attack and arrhinias. When a patient hits the critical stage of CVD, their heart is no longer able to pump blood effectively through the body. This is end-stage heart failure, the point where no medications or treatment options are effective, and the only option is a heart transplant [33]. It is reported that every year around 5000 heart transplants are performed, for every 50,000 people that need a heart [33]. Even for those fortunate enough, this surgery requires patients to remain on a lifelong regiment of immunosuppressant medications. Cardiac tissue engineering presents a unique opportunity to overcome complex hurdles and develop methods and materials that can repair or replace damaged tissue and requires a deep understanding of cardiac structure and function as well as cellular interaction with biomaterials.

2.1 Current Approaches

One of the first innovative approaches was to use stem cell-based therapies where cells are delivered either via intramyocardial delivery or intracoronary injection. A clinical trial using c-kit(+) cardiac stem cells showed significant improvement in global and regional left ventricle function, a reduction in infarct size, and an increase in viable tissue that persisted for a year post procedure [34]. A study using intracoronary administration of autologous cardiosphere-derived cells also led to a decrease in infarct size, increased viable myocardium, and improved regional function of the damaged myocardium for over a year [34]. However, despite advancements, there is still no meaningful clinical data showing stem cell therapies are a viable solution [35]. Most clinical trials have been small, and results are inconclusive [35].

In recent years, gene therapy as emerged as the first generation of cardiac regenerative medicine [36]. Using viral vectors, adeno-associated virus / lentivirus, plasmid DNA is delivered into cells to restore levels of a target protein [36]. Studies have shown successful transfer and expression of the desired protein resulting in reversal of damaged tissue [36, 37]. However still, there are many trials that were not able to show positive results, reportedly, gene transfer efficiency being the biggest problem [36, 37]. While the technology is exciting, it is still new. The risk of off-target effects, tumorigenesis, and arrhythmogenesis among other safety concerns are huge hurdles to overcome and will need to be addressed before it could be considered a potential treatment [36]. Other approaches are being developed integrating cell biology, biochemistry, material science, and mechanical & electrical engineering, to achieve a desired outcome [37]. The most notable of these being cardiac patches and hydrogels.

2.1.2 Cardiac Patches

Cardiac patches are typically circular or square shaped platforms made from a biomaterial combined with cells. They are meant to be surgically implanted directly onto the ischemic zone of a damaged heart to restore structural function while providing cells with an environment for cell growth [38]. These patches must be able to adhere to the surface of the tissue to maintain structural integrity during contraction [38]. Ideally, these patches would match that of native healthy tissue, with a Young's modulus between 8-15 kPa [38]. In addition to mechanical considerations, biomaterials must conduct electric signals promoting the hearts contractions [38].

Furthermore, they need to have a biodegradation rate that is consistent with the formation of new tissue that is being integrated [38]. There have been several cardiac patches that have gone to pre-clinical and clinical trials that have shown promising results. Jackman et al 2018, engineered 1 x 1 cm^2 cardiac tissue patches out of neonatal rat ventricular cells, poly-dimethysiloxane (PDMS) tissue molds, and a fibrin Matrigel hydrogel mixture. They implanted patches onto rat hearts which after two weeks in culture, we able to achieve a higher contraction force of 18.0mN and higher conduction velocity of 32.3 cm/s [39]. While these improvements along with the patches ability to maintain local tissue structure were encouraging, it was also noted that there was no change or improvement in electrical conductivity of the region [39].

Some patches have entered clinical trials in animal models, however the major issues facing the commercialization of these applications is the number of cells that can survive and integrate into the infarct region is very low [38]. Material limitations are also an issue where matches historically cannot achieve good electrical coupling after transplantation and end up detaching causing arrhythmias [39]. Additionally, limitations in size restrict use to small animals [39]. Finally, the greater issue is these applications require open-chest surgery, carrying its own set of complications as well as the possibility of increasing the damage to the infarct area.

2.1.3 Injectable Hydrogels

Hydrogels are 3D cross-linked biomaterial networks that can be injected in a liquid form and solidify after being exposed to a controlled stimulus. Regenerative medicine has long favored hydrogels for their ability to be tuned physically, chemically, and mechanically [38]. In the cardiac space, injectable hydrogels are of great interest as they circumvent the previously mentioned surgery required for cardiac patches. In or this to be achievable, hydrogel materials must have transformability, or the ability to transition from an aqueous phase to a solid form, which is essential for delivery [38]. In liquid form, hydrogels can be injected directly into the site if injury, cross-link, and then provide a physical interface for cell regeneration and mechanical stability. These materials can encapsulate therapeutic cargo, i.e. cells, as they rapidly undergo a phase change responding to temperature, pH, light, or other forces [39]. Because of this, stimulus responsive hydrogels can overcome the hurdles of other methods such as patches, as a minimally invasive technique able to directly deposit the therapeutic material onto the infarct area [38]. As with all approaches, materials should be biocompatible and biodegradable and possess the necessary mechanical and electrical properties [38]. Not only is this critical for the development of the cells, but the material must also be able to integrate and replicate the properties of native tissue and withstand the forces it is subjected to.

2.2 Scaffold Materials

A wide range of materials, both biological and synthetic, can be utilized, and tuned for individual applications each with their own level of biocompatibility, clinical relevance, and biological functionality. Their composition, structure, and mechanical properties can be tuned to replicate the native complex network of the ECM, regulating cellular behavior. However, material limitations, stability/degradation, vascularization, and scalability must be overcome to achieve clinical relevance.

There are two major classes of material that can be used, natural and synthetic, each with specific advantages and disadvantages. Natural biopolymers are made up of proteins derived from living organisms of which include, collagen, fibrin, alginate, gelatin, keratin, fibroin, silk and more [37]. These materials are highly advantageous because of their ability to retain their biological properties [37,38]. Their biocompatibility and degradability give them a huge advantage in clinical applications that other materials have yet to match. It has already been shown that natural hydrogels can restore function while suppressing ventricular remodeling with low immune responses in animal models which has led the way to numerous clinical trials [38]. Furthermore, these materials can be enzymatically degraded by cells which provides major advances for new tissue to develop within the scaffold, integrate with native tissue, and have the hydrogel break down naturally leaving behind newly formed tissue [37]. However, their efficacy is significantly hindered by their lack of mechanical properties, required for cardiac regeneration and are electrically inert, limiting cell-cell communication.

Synthetically produced hydrogels on the other hand offer many advantages due to the level of control over physical and chemical properties. Materials, such as polyethylene glycol (PEG), polyvinyl alcohol (PVA), polylactic acid (PLA), and more, can be engineered to have very specific mechanical properties in terms of stiffness, porosity, and hydrophobicity, allowing the hydrogel to match native tissue [38]. Unlike natural hydrogels, their degradation can be controlled with more predictability, giving a stable scaffold for the required amount of time. In terms of manufacturing, they have a much higher level of reproducibility and consistency, reducing batch-batch variability, and easier to scale in a clinical setting [38]. Despite their material advantages, being synthetic, they lack the bioactive molecules of natural hydrogels which greatly affects major cellular processes that are trying to be replicated. In addition, their biocompatibility and toxicity still have a long way to go.

2.2.1 Fibrin & Collagen

Fibrin has long been known for its role in the wound healing cascade, blood clotting, and inflammatory responses. Fibrin fibers serve as a natural scaffold for tissue regeneration and promote cell migration and tissue regeneration. In response to tissue damage, fibrin fibers are formed to serve as a natural scaffold for tissue regeneration when fibrinogen is catalyzed by the clotting enzyme thrombin [40]. Secreted by the liver, fibrinogen is a fibrous 340 kDa dimeric glycoprotein composed of ~138 amino acids. The molecule is a symmetrical dimer, composed of three domains: two outer identical D-domains linked by a central E-domain, containing three fibrinopeptides alpha, beta, and gamma [40]. Thrombin, a serine protease, has a high specificity for the alpha and beta chains, and cleaves fibrinopeptide a, exposing a tripeptide at the N-terminus creating what is known as a “knob” [40]. Complimentary to this is a “hole”, located in the center of the outer D-domains. Fibrinopeptide B is cleaved much slower and while not integral to polymerization plays a large role in lateral aggregation [40]. Once fibrinogen is cleaved into a fibrin monomer with two strands exposed, they become highly reactive forming oligomers until they become a double stranded protofibril roughly 600-800 nm in length [40]. These protofibrils then begin to aggregate forming thick fibrous fibrin strands [40]. This polymerization process forms a three-dimensional fibrous network that can be used to encapsulate and culture cells.

As a scaffold material the main advantages are its biocompatibility, bioresorbable, and ability to incorporate cells into its matrix. It has natural binding sites showing a high affinity for various biomolecules and surfaces, as well as growth factors [41]. Specific properties such as thickness and length can be tuned based on ionic strength, pH and concentration, and with its high area/volume ratio, giving it the ability to mimic specific microenvironments [41]. Biomaterials based on this polymer can be prepared readily, are already in clinical use, and have a range of tissue engineering applications [41,42].

Collagen is one of the most abundant proteins in the body, and a major component of the ECM responsible for load carrying and pressure resistance [41-43]. Over 20 varieties are known, the most prevalent being type I, making up 90% of the total collagen in the body [43]. Like fibrin, collagen is a glycoprotein and has a molecular weight of ~300KDa [44]. Collagen structure varies on the tissue is found in, i.e. skin, bone, tendon, ligaments, cornea, internal organs, but with all structures is typically made up of ~1000 amino acids forming three left-handed helices that twist together to form the collagen molecule [43,44]. Like fibrin, collagen has high biocompatibility, biodegradability, cell adhesion, and biological recognition sites.

2.2.2 Hybrid Hydrogels

Both materials have been used extensively as natural biopolymer 3D scaffolds to culture a range of cells, owing to their previously mentioned biocompatibility, degradability, high density of binding sites, non-toxic byproducts, and off the shelf availability. Even as simple, single protein constructs, they can recapitulate enough of the native cellular environment to sustain and develop advanced cultures. However, only recently have these two materials been used as co-cultures. It has been demonstrated that during polymerization the two protein networks develop independently of one another, ultimately forming a scaffold that combines the advantageous properties of both proteins.

Differences in fibrin collagen mechanical properties combine both structural support and elasticity for cells during development and proliferation. Collagen offers a rigid, organized structure, promoting cell alignment and mechanical stability, while fibrin offers a soft dynamic environment needed in early-stage tissue repair for cell migration and proliferation. Ideally this gives cells the rigidity and structural support, while fibril offers elasticity for the developing tissue. Collagen has been shown to enhance ventricular cardiomyocyte maturation owing to its stiffness. ECM stiffness is critical for cellular adhesion, alignment, and motility [48]. It has been demonstrated that in rat ventricular myocytes maturation is dependent on this property [48].

Fibrin offers unique mechanical properties, viscoelastic characteristics, strain hardening, that make it stand out from other protein polymers. It has been shown to be highly elastic and extendable, up to 4x longer than its relaxed state before breaking [49]. Furthermore, stretching a fibrin network results in fiber densification and aggregation by the expulsion of water [49]. This viscoelasticity mimics the natural myocardium as it is characterized as a non-linear viscoelastic material itself, exhibiting stiffness depending on the rate and magnitude of stress or compression [50]. In the heart, sarcomeres stretch from 1.8 μm to 2.1 μm as they transition from diastole to systole, and at their max extension, non-linear stiffening is due to fiber alignment of titan and collagen thus determining myocardial stiffness [50]. The ability to mimic these viscoelastic properties, allows for controlled mechanical loading and unloading during contraction in culture [50].

Integrin binding sites are critical for cellular adhesion and signaling. Integrins are transmembrane proteins responsible for the extracellular linkage of the cell’s cytoskeleton with the ECM. They recognize oligopeptides present on ECM components and function not only in anchoring the cell, but the transmittance of bidirectional signaling. Integrins are composed of an alpha and beta subunit that can be assembled into a combination of 24 different heterodimers with varying specificities towards the ECM [51-54]. In cardiomyocytes, integrin heterodimers α1β1, α5β1 and α7β1 are the most ubiquitous, binding to collagen, fibronectin, and laminin respectively [51]. Attachments via integrins are localized in costemere and anchors the muscle Z-disc with the sarcolemma membrane [51]. In addition to adhesion, these junctions are a key component in mechanotransduction, or the ability to interpret mechanical signals and output biochemical signals [3]. The mechanical force applied to an integrin is channeled throughout the cell over the cytoskeletal network, reaching all the way to the nucleolus [51]. This is a key point of how ECM composition influences cell and tissue development.

Collagen contains several motifs that facilitate integrin binding that are crucial for cell-cell and cell-matrix interactions. Tight packing of the right-handled triple helix comes from collagens primary sequence, a (Xaa-Yaa-Gly)n triplet repeat [52]. Crucial for structural integrity of connective tissue. "Xaa" and "Yaa" are often proline and hydroxyproline respectively, where "Gly" is glycine. In the Xaa and Yaa positions, amino acid side chains face outside the helical surface presenting an opportunity for intra-helical interactions [52]. There are four known collagen binding integrins, α1β1, α2β1, α10β1, and α11β1, which have different affinities for different types of collagens [52].

In the natural cardiomyocyte ECM, fibronectin and vitronectin provide an oligopeptide binding site called "RGD" comprised of Arg-Gly-Asp [53]. The recognition of this site is also present on fibrin and plays an important role during heart development [53]. RGD recognizes α5β1, αVβ3, and αVβ5, where the α5 unit is a predominant integrin in fetal and neonatal cardiomyocytes [53]. Additionally, the α5β1 and αVβ3 has been found to become stronger when force is applied [53]. These interactions have been shown to induce the activation of survival pathways, PI3K/Akt, and MAPK signaling involved in the regulation of contractility [53]. αVβ3 integrin binding to RGD sequences has been shown to influence cardiomyocyte contractility and calcium handling, which are vital for maintaining proper heart function [53].

Despite their combined benefits, fibrin and collagen as all natural biopolymers suffer from overall mechanical weakness and are electrically inert. Next generation scaffolds seek to overcome the mechanical and electrical limitations of biopolymers by integrating nanostructures derived from gold carbon into the matrix. Carbon nanotubes (CNTs) provide such a with their unique mechanical strength and conductive properties [53].

2.3 Nanomaterial in Cardiac Tissue Engineering

Recent studies have demonstrated that the incorporation of nanomaterials can overcome the limitations of conventional hydrogel scaffolds. Nanomaterials are defined as having structural properties on the nanoscale between 1 and 100nm. At this size, materials exhibit unique physical, chemical, and biological properties, different from their original bulk counterparts. Their inherent anisotropy and high surface area-to-volume makes them uniquely suited to incorporate into biological systems and influence electrical conductivity, hardness, and topography, improving tissue functionality [54]. These changes in electrical, mechanical, and thermal properties, can not only have a therapeutic effect on, but drastically influence hydrogel bulk properties in terms of conductivity and stiffness. This ability to transmit electric mechanical, electrochemical, and electroactive stimulation through an otherwise electrically inert construct is crucial for the integration of cells and scaffold into the myocardium's electrical syncytium.

When looking at cardiomyocyte development, there are several genes and signaling pathways relevant to the interactions between nanomaterial and the cells [54]. During development, cardiac transcription factors Tbx5, Nkx-2.5, and GATA-4 are activated influencing structural genes such as myosin heavy chain, desmin, cardiac troponins, and myosin light chain [54]. Signaling pathways involved in differentiation include, BMP, FGF, Wnt, and TgfB/Activin/Nodal pathway [54]. Fetal and neonatal cardiomyocytes from rats and mice are often used due to their availability and regenerative capabilities [54]. Neonatal cardiomyocytes in their early stages have a high survival rate and greater regenerative capabilities compared to adult cells and are a very good model for testing nanomaterials to improve their survival and function in vitro [54].

2.3.1 Carbon Nanotubes

Carbon nanotubes (CNTs) are cylindrical structures made of a single layer of graphene arranged in a hexagonal pattern. They can be synthesized by electric-arc discharge, laser ablation, as well as several different chemical vapor deposition (CVD) methods [54]. There are three classes of CNT which indicate their structure, single-walled, double-walled, and multiwalled [54]. Single walled carbon nanotubes (SWCNT) can be described as a single sheet of graphene seamlessly rolled into a cylinder. Diameters range from 0.8-2nm, lengths on the µm scale and tensile strengths of 11–200 GPa, Young's modulus of 0.27–1.34 TPa, electrical conductivity of 104

S/cm, and thermal conductivity of 5000 Wm^{-1} K) (29,30), while MWCNTs have diameters reaching ~100 nm [54].

Many studies have demonstrated the efficacy of incorporating CNTs into hydrogels and cardiac patches for improving electrical and mechanical strength. Shin et al 2014 seeded neonatal rat cardiomyocytes onto CNT incorporated gelatin methacrylate (GelMA) [55]. They demonstrated cells grown on CNT hydrogels showed 3 times higher spontaneous beat rate and 85% lower excitation threshold [55]. This study also demonstrated higher expression of troponin I and Cx43 with no toxic effects observed after 7 days [55]. Yu et al used carboxyl-functionalized multiwalled CNTs with collagen (rat tail) type I to culture neonatal rat cardiomyocytes. They demonstrated the mechanical and electrical improvements with CNT incorporated gels influenced and improved cell contractions [56].

In addition to CNTs, other carbon-based materials have been used including carbon nanofibers (CNFs) and graphene and its derivatives. Fabricated by CVD or electrospinning, CNFs have a higher aspect ratio with diameters ranging from 50-500um and lengths in the micron range [56]. They possess unique physical and mechanical properties with tensile strength of ~3GPa, a Young's modulus of 500 GPa, thermal conductivity of 1900 $Wm^{-1}K^{-1}$, and electrical conductivity of approximately 103 S/cm [56].

2.3.1 Gold Nanomaterial

Gold nanostructures have been promising material candidates due to their high electrical conductivity, nanoscale architecture, and minimized cytotoxicity [57]. When synthesized, they can be made into different shapes and configurations, such as nanospheres, nanorods, tripods, tetrapods, nanotubes, and nanocages, as well as formed into fibers, films and shells [57]. These unique shapes have been reported to result in unique specific absorbances, beneficial to diagnosis, sensing, molecular imaging and stem cell tracking [57]. As with other nanomaterials, they are also used to enhance the electrical conductivity of nanocomposites [57]. Because of these properties, as well as biocompatibility, ease of surface modification, and optic properties, these have long been used in cardiac tissue engineering [57].

AuNPs have been used to improve the electrical conductivity of scaffolds for cardiac tissue engineering in several areas. They have been used in omental patches that, when incorporated, cells showed elongated and aligned morphology as well as increased Cx43 expression and increased contractile forces [39]. Another study integrated AuNPs into electrospun fibers to produce a nanocomposite scaffold [39]. Cells grown in these cultures also exhibited greater alignment, elongation, and higher expression of a-actinin, and increased cellular contraction amplitude [39]. Hydrogel AuNP composites have also been shown to have high efficacy due to their ability to be homogeneously dispersed, and able to mimic physiological properties of the native myocardium [39,57].

2.3.3 Silicon Nanowires

Silicon nanowires (SiNWs) are 1D semiconducting nanostructures that have exceptional mechanical and thermal properties. SiNWs are commonly produced by vapor-liquid-solid (VLS), a bottom-up growth mechanism that refers to vaporous silicon passes through a liquid droplet to form a solid product [58, 59]. Briefly, a particle such as gold, is placed on a Si substrate and brought to a temperature (above 363°C) where the Au/Si system forms alloy liquid droplets [60]. These droplets are then exposed to a silicon gas precursor, such as silane (SiH_4) or silicon tetrachloride ($SiCl_4$), which flows through the reaction chamber [60]. The gas diffuses into the molten metal catalyst droplet which becomes supersaturated, at which point silicon freezes out at the silicon/droplet interface, leading to the growth of the wire [58-61]. Growth techniques range from chemical vapor deposition (CVD), molecular beam epitaxy (MBE), laser ablation, electrochemical deposition, as well as solution-based methods [58,59]. The electrical properties of these wires can be modified by introducing impurities during growth. Doping by the introduction of phosphine (PH_3) and diborane (B_2H_6) gas, creates n-type and p-type nanowires respectively [59]. Owing to their stability and biocompatibility in biological systems as well as their manufacturing scalability they have long been used as biosensors, field-effect transistors, and drug delivery mechanisms [60,61]. Tan et al. 2016, demonstrated the incorporation of SiNWs into an organoid culture of hiPSC-derived cardiomyocytes [59]. They were able to show the presence of SiNWs significantly improved the structural organization and electrophysiological properties of cardiomyocytes grown in these cultures. These cells showed better alignment, calcium handling, and action potential characteristics than those cultured without SiNWs [58,59]. However, despite their advantages as a biomaterial there is little published on work done incorporating them into hydrogel material when compared to other nanomaterials.

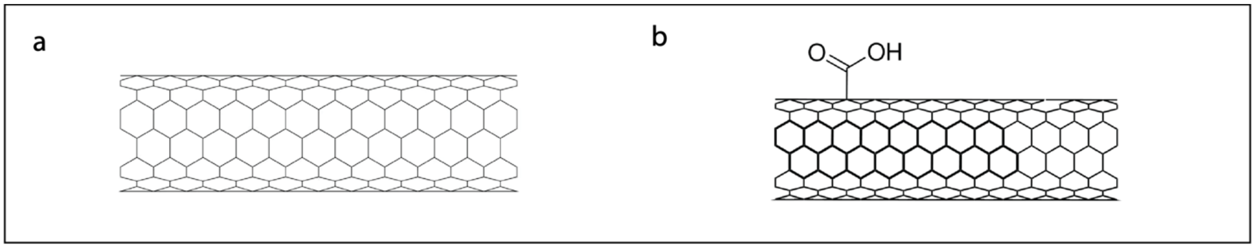

FIGURE 2 SINGLE WALLED CARBON NANOTUBES. A) PRISTINE SWCNT. B) CARBOXYLIC ACID FUNCTIONALIZED SWCNT.

3. Carbon nanotube Dispersion

Carbon nanotubes (CNTs) have distinct physical properties making them challenging to uses in biological systems due to their poor solubility and tendency to aggregate. First, de-bundling must be accomplished to overcome the strong van der Waal forces causing aggregation, separating them into individual tubes also known as exfoliation. Secondly, they must be modified in such a way that allows them to integrate into a biological system without causing adverse cellular responses and cytotoxicity.

The first step in this process is the modification is the addition of a functional group to the side wall, which is typically carboxyl, hydroxyl, or amine. This functionalization lowers the Van der Waals' forces between CNTs, mitigating the amount of energy required for de-bundling and increasing the CNT-matrix/solvent interactions for further modification. To accomplish this, chemical treatment is a common method of functionalization, namely acid oxidation. CNTs are immersed in a mixture of nitric and sulfuric acid with a ration of 3:1 and refluxing the mixture for several hours at a high temperature (60-123°C) [62]. During acid oxidation, the carbon-carbon bonded network of the graphitic layers is broken, allowing the introduction of oxygen atoms in the form of (in use for this work) a carboxyl group. CNTs are washed several times with dH_20 to remove the acid and neutralize, until a final pH of ~7.1 is reached [62,63]. This results in the carboxylation of the CNT side walls without damaged their optical or thermal properties, as seen in [Figure 1] [62]. In lieu of performing this reagent and time intensive process, single-walled carboxylic acid functionalized carbon nanotubes were purchased from Sigma-Aldrich. These SWCNTs were used as the starting material for the disperse solution being prepared for hydrogel use. Their bundle dimensions are D x L 4-5nm x 0.5-1.5 µm. From the manufacturer these off the shelf CNTs contain 5-8% metal impurities which were removed during the dispersion process by purifying with several centrifugation and dialysis steps.

Once functionalized CNTs can be more easily dispersed into solution, however they must then be further modified for use in biological systems. Here, they will be interacting with culture media, buffer systems or other physiological fluid containing a variety of organic molecules, high salt concentrations, all of which highly affect solubility. Because of this, CNTs must be modified to interact with such systems and not form agglomerations. This presented a unique challenge as the requirement for this work as CNTs would need to be dispersed in a buffer system used in the hydrogel formulation and relevant to future cell culture work. The carbon nanotube suspension would need to be stable at a high enough concentration to be effectively diluted into the hydrogel formulation, in addition to being biocompatible.

To solve this problem, the carboxylated SWCNTs would first need to be dispersed into an aqueous solution. Commonly, surfactant aided dispersion under the application of external energy (sonication) is used to separate the bundled nanotubes by overcoming their strong Van der Waals attractions. Bile acids (BAs) a physiologically important biosurfactants that are commonly used for solubilization of drugs and hydrophobic polymers and can outperform many commercial surfactants [55]. The solubilization ability of BAs is a result of their amphiphilic chemical structure that is fundamentally different from other surfactants. This nonconventional amphipathic structure has a convex hydrophobic side, a concave hydrophilic side, and a negatively charged head attached to a side chain [66]. This allows for molecular packing onto the surface of the CNT, where the hydrophobic art interacts with the nanotube surface and the hydrophilic interacts with the buffer system. Unlike linear surfactants such as sodium dodecyl sulfate (SDS), these unique structural properties make it an effective dispersant of biological molecules in living cells [66]. Sodium deoxycholate is one such bile salt that has been commonly used and was selected for this application. A concentration of 1% w/v was chosen based on literature references [67-69]. A strong probe sonicator must be used over bath sonicators because of the power required to break apart the nanotubes. The metal tipped probe is inserted into the sample itself and emits high-frequency ultrasonic energy directly into the sample, causing localized cavitations.

As these dispersions are being used in biological systems, further modification is required to address the issue of cytotoxicity. Here, bovine serum albumin (BSA) is commonly used to improve the biocompatibility of carbon nanotubes as well as improve dispersion [65]. BSA has long been a model protein owing to its structural stability and range of biological applications [65]. Derived from bovine blood, BSA is non-toxic, biocompatible, and very stable in physiological conditions (temperate and pH). When sonicated with carbon nanotubes, BSA will bind through hydrophobic interactions and π–π stacking coating the nanotubes [65].

When adsorbed onto CNT's, BSA acts as a stabilizing agent through non-covalent interactions, preventing aggregation and acts as a barrier between the nanotube and the environment. Hydrophilic residues are left exposed to the buffer system and steric repulsive forces prevent the re-aggregation of CNTs. The resulting dispersion then benefits from increased biocompatibility, with defect-free, highly stable carbon nanotubes [65].

This would be the foundation for the dispersion strategy used for this work. First, dry SWCNT powder is first weighed carefully on a scale protected from air movement. The nanotubes are then wetted with the sodium deoxycholate buffer, mixed, and moved into a 15ml conical tube. An ice bath contained in a Styrofoam box is then set up with a custom lid that tightly fits the tube, which is held into place with parafilm. The sonicators probe is then positioned precisely in the sample and is ready for use. Here a Branson probe sonicator was used. Because the volume of these samples was small (typically around 8ml), a microtip attachment had to be used on the sonicator. This restricts the amount of power the machine can deliver to 40% capacity. This resulted in roughly 45-55 watts being delivered into the sample. Here it should be noted this is the first experimental limitation. Commercially, CNT dispersion is done under much stronger sonication power, roughly 200-500 watts. Through trial and error, it was discovered that a pulse setting of 5 second off, 2 seconds on would keep the sample at a low enough temperature. The total on time for this step is one hour. A second sonication step was then done with the addition of BSA. A concentration of 10x that of the weighted SWCNT would then be added and sonicated in the same manor for an additional hour.

After sonication, the mixture was centrifuged for one hour to remove impurities, unbound BSA, and excess nanotube bundles. The final step in sample preparation involved a buffer exchange via dialysis, which facilitated the dissociation and removal of sodium deoxycholate from the nanotubes. Samples were dialyzed against the predominant buffer later used for hydrogel protein (fibrin), 20mM HEPES 0.9%. There were three dialysis steps. Each volume was over 500x the total sample volume and set for 4 hours at 4C with the final step being left overnight. The following day a final 21,000X centrifugation step was done to remove all final aggregates producing the final dispersion. With the samples ready for use, they must then be characterized to assess quality and define properties.

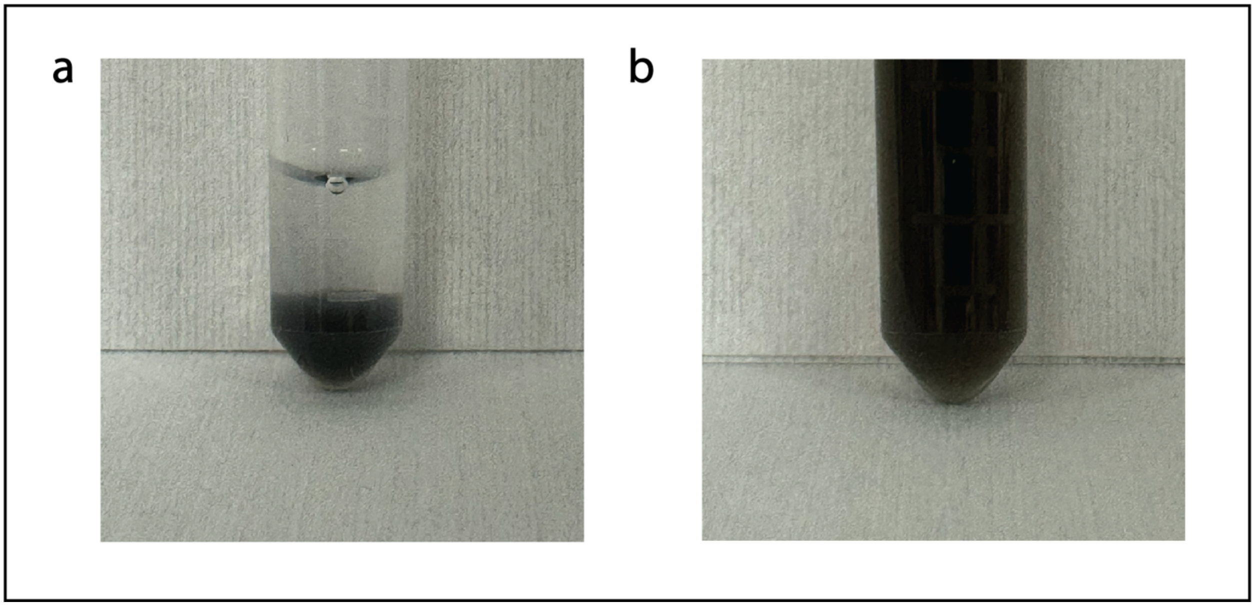

Figure 3 **SWCNT dispersion. a) non-dispersed SWCNTs. b) Fully dispersed SWCNTs.**

3.1 Concentration

Concentration is the first crucial aspect to define when creating dispersions as 100% of the as weighed CNT powered is never completely dispersed. Due to impurities or limitations of the dispersion methods, bundled CNTs are removed during centrifugation steps [70]. Some literature references dry and weigh the removed CNT pellet however this method has been shown to not as accurate as UV-Visible spectroscopy. First, a standard curve must be generated by dispersing a test sample. A small concentration of 0.1mg/ml is used to disperse as much of the nanotubes as possible. This test sample is sonicated thoroughly for 1 hour and then measured with UV-vis without centrifugation in an effort for the absorbance to be as accurate as possible. A full spectrum measurement was taken between 200-800nm range to determine if there is any interference or artifacts and if so where. A wavelength of 600nm wavelength was selected for future measurements. Next, serial dilutions were made with 10 points, measured and recorded [Figure 4.]. With the standard curve complete, all future dispersions could be diluted, and an accurate concentration determined providing it is within the curve’s limits.

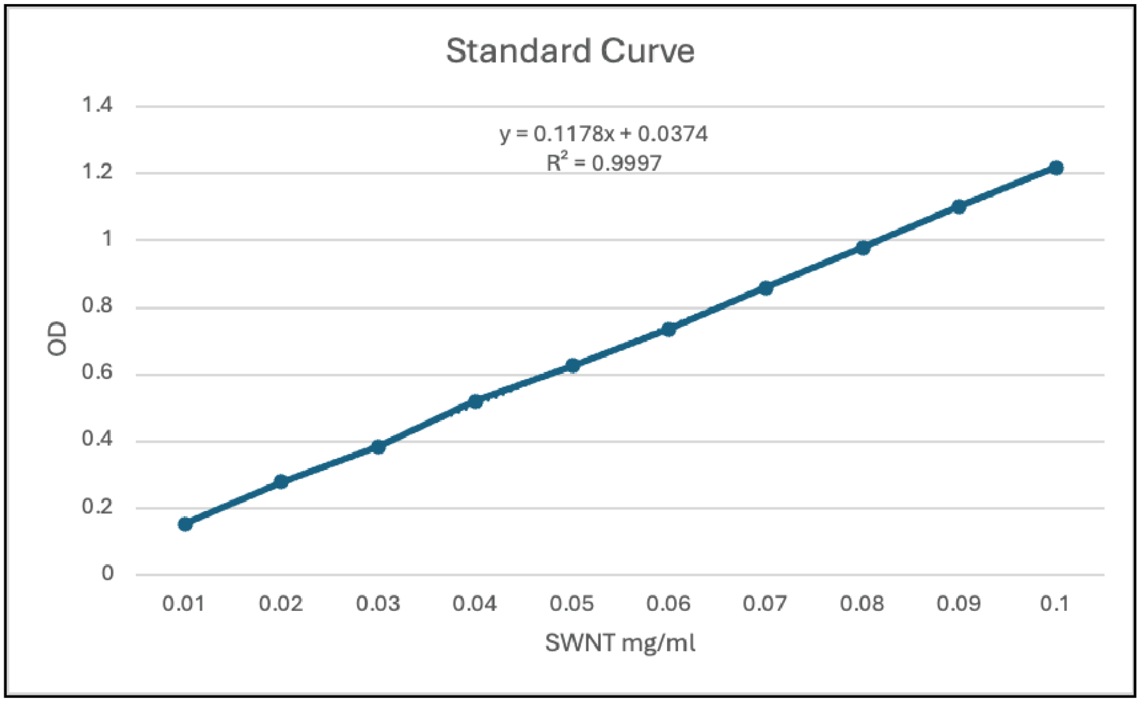

FIGURE 4: 10-POINT STANDARD CURVE MEASURED BY UV-VIS.

3.2 Dynamic Light Scattering & Zeta Analysis

Dynamic Light Scattering (DLS) is widely used to characterize the size distribution and dispersion state by measuring scattered light as particles undergo Brownian motion. For carbon nanotube solutions, this can give important insight into the quality and purity of the dispersion. This technique measures the hydrodynamic ratio of molecules diffusing in solution by converting scattered light to particle size distribution [71]. As thermal energy drives the random motion of the particles in solution, movement is influenced by particle size, the solution viscosity, and temperature. Using a laser, DLS can measure the random motion of these particles in relation to one another on a very short time scale as they continue to move and undergo exponential decay. If the particles were completely still, the measured intensity would be constant, however as the particles move the intensity fluctuates over time. The combination of all particles in a solution creates a fluctuating intensity signal which depends on the diffusion rate. Snap shots of the change in light intensity over time are taken very quickly (nano or microseconds) and compared back to the original measurement. Starting at t=0, the coloration value is 1, which would be a perfect fit, and as time goes on, the larger the difference in intensity fluctuations and values go to zero. Here, the intensity signals can no longer be correlated with the original signal. The larger the particles the longer it takes for them to diffuse, and the longer it takes for a complete loss of the coloration signal. [Figure 5.] shows an example of this with real world data in a graph called a correlogram.

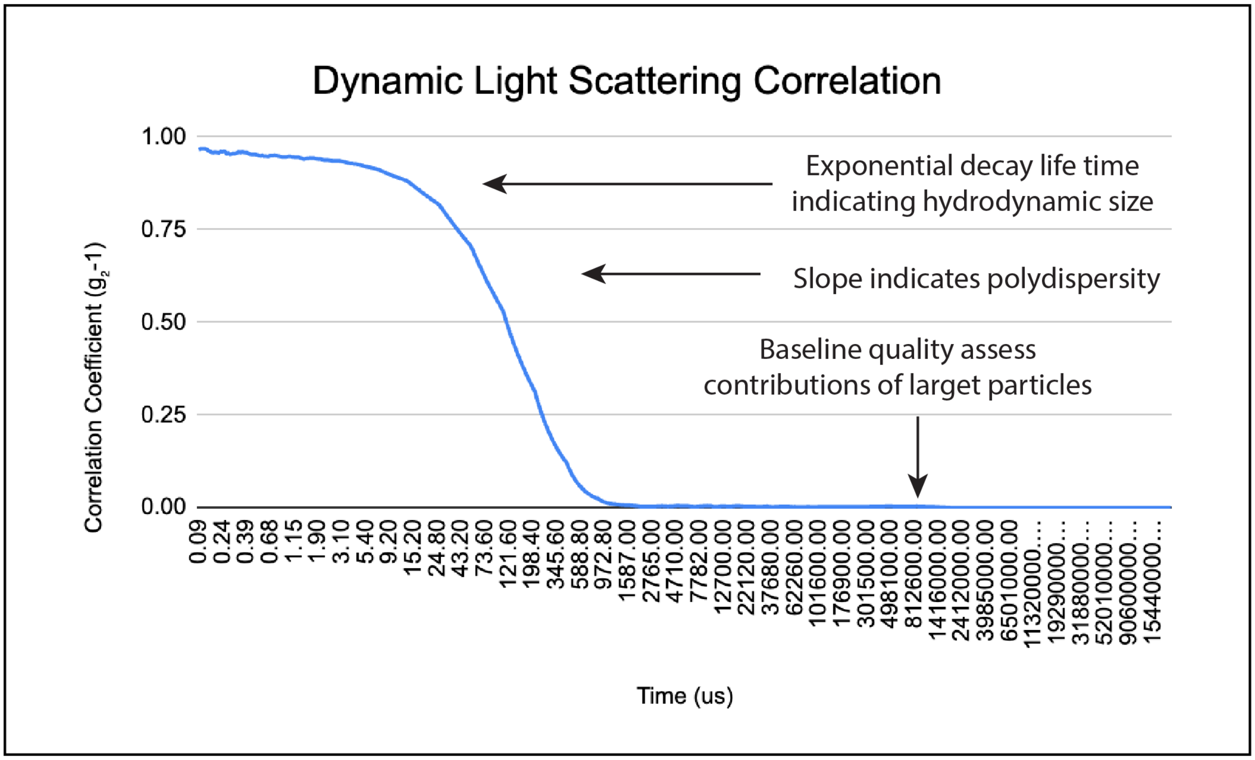

FIGURE 5. RAW CORRELAGRAM DATA FROM SWCNT + BSA DISPERSION.

The information obtained from measuring the fluctuations in light intensity is then used to calculate particle size. This data is fit to an algorithm to determine diffusion coefficient, then applied to the Stokes-Einstein equation to obtain the particle size [71,72].

$$d_H = \frac{k_B T}{3\pi\eta D}$$

dH = hydrodynamic diameter, k = Boltzmann’s constant, T = absolute temperature, n = viscosity, and D = diffusion coefficient. Therefore, using DLS, the size of all particles in a solution can be measured and visualized as an intensity distribution showing the intensity of scattered light as it results from each size population. The resulting hydrodynamic size is the diameter of a sphere that diffuses in the same manor of the sample being measured. Therefore, particles that are aggregated will show a different hydrodynamic size than those that are not. This size reflects not only the core particle, but any ions or polymers bound to its surface as well. To that end, particles that are not spherical, in this case tubular, will give a result based on how the particle moves, but determining their size is not as straight forward. The size can still be determined through various equations [71,72], however here, where size isn't being evaluated, DLS can be a fast and easy method for evaluating the homogeneity of the dispersion.

In DLS, the polydispersity index or PDI is used for measuring the heterogeneity of particle size. This number is an indication of the uniformity in the particle size distribution. A low PDI means the particles are monodisperse and uniform in size, and a parver PDI indicates a large size distribution or polydisperse and would be indicative of poor dispersion quality. As the manufacture reports, <0.1 is highly monodisperse, 0.1-0.25 is monodisperse, >0.25 indicates polydisperse or aggregates, and >1 is not appropriate for DLS analysis.

A Malvern Zetasizer - Panalytical Advance Ultra Red Label was used to take DLS and zeta potential readings. Samples were diluted 20x, with the machine then taking three readings, the resulting average of which was used. Here it can be demonstrated that the dispersant sodium deoxycholate, and unbound BSA was removed with dialysis, as well as effectively removing a large majority of remaining aggregated SWCNT bundles. First [Figure 6.a,b,c] shows the removal of the 1% sodium deoxycholate, via dialysis. [Figure 6.a] shows an overlay of the pre-dialysis sample against the buffer. Here, multiple peaks can be observed from smaller ~2-4nm monomers to larger in the 4700nm + range. After sonication, the smaller peak disappears with the assumption these monomers have adhered to the CNT sidewall, and the larger unbound micelles remain visible. Once dialyzed, weak non-covalent binding of sodium deoxycholate molecules will disassociate and be removed along with the larger micelles. As the dispersion is centrifuged before dialysis, excess BSA and larger CNT bundles are already removed from the sample, which can be seen by the lack of excess peaks.

Removing non-disperse / aggregated nanotube bundles is a critical final purification step. To demonstrate the importance of centrifugation speed two aliquots of the same post dialysis dispersion were centrifuged at different speeds, 4950xg and 21,000xg. In [Figure 6,d] a large shoulder is evident at the beginning of the peak. In [Figure 6, d,e,f] it is shown how post dialysis centrifugation is required as a final purification step removing non-disperse / aggregated nanotube bundles. When aliquots spun at 4850xg showed broader peaks with a large shoulder, aliquots spun at 21,000xg show the elimination of the shoulder and tightening of the peak. [Table 1] corroborates these graphs, as we see the Z-average drop from 115.5 to 96.35 suggesting the centrifugation speed was able to remove even more bundles from the sample. This is confirmed by PDI drops a significant amount from 0.249 to 0.209, suggesting a much more homogonous sample. With the results, we can conclude that the sodium deoxycholate, unbound BSA, and harmful aggregates were removed from the sample. The resulting SWCNT dispersion contains successfully exfoliated nanotubes that are monodisperse and stable in suspension.

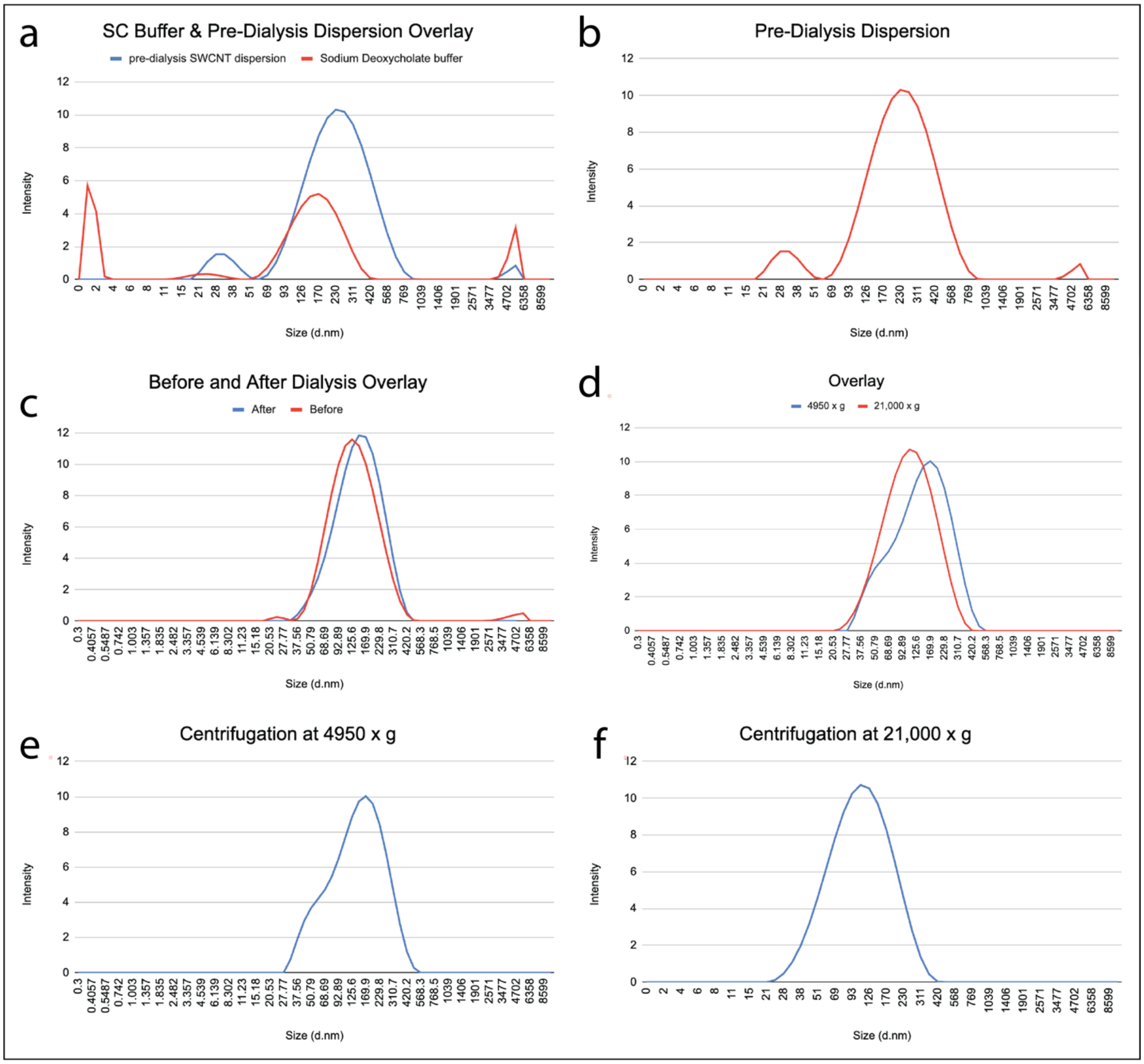

FIGURE 6 DYNAMIC LIGHT SCATTERING.

Zeta potential is another important aspect for characterization and understanding the stability of the dispersion. Zeta potential measuring the difference between the charged surface of the nanotube and surrounding medium and reflects the electrostatic repulsion between particles. The strength and polarity of this layer are represented by the Zeta potential which is typically expressed in in volts. A high Zeta potential is considered over +_ 30mV, moderate between 10 and 30, and low under 10.

Samples prepared with the sodium deoxycholate/BSA strategy consistently averaged ~ -17mV and were stable for roughly 6 months when stored at 4C. These results are consistent with what sodium cholate and sodium deoxycholate can produce in the literature notably around -15mV [60]. While detergent surfactants such as Pluronics, Triton X-100, SDS, and NaDDBS can produce dispersion between -40-80mV, they are significantly more cytotoxic and harder to remove so they were never considered [74]. These results are likely close to the limitation that could be produced. As previously mentioned, the major limiting factor was the amount of power able to be delivered from the sonicator into the sample. Had a more powerful machine been available, it is likely a higher Zeta potential could have been achieved.

TABLE 1. DYNAMIC LIGHT SCATTERING & ZETA ANALYSIS

	Concentration (mg/ml)	**Z – average (nm)**	**PDI**	**# of peaks**	**Zeta Potential (mV)**
Pre-dialysis	3.2	181.4	0.412	3	NA
Post-dialysis 4850 x G	3.1	115.5	0.249	1	-17
Post-dialysis 21,000 x G	2.9	96.35	0.209	1	-17.1

3.3 Fourier Transform Infrared Spectroscopy

As previously mentioned BSA is an important aspect of creating a biocompatible SWCNT dispersion. Because of this, it is important to characterize the interactions between BSA and SWCNTs to ensure the protein has indeed bound to the nanotube sidewalls. Here, Fourier Transform Infrared Spectroscopy or FTIR, can be fast, non-destructive technique, that requires minimal sample preparation and small volumes in which to do so. FTIR can identify functional groups on the BSA molecule as well as the CNTs and changes in which can indicate binding or lack thereof.

While the interactions are not straightforward, hydrophobic forces and non-covalent bonding cause the adsorption of BSA onto the SWCNTs. Li et al. showed that the interactions between BSA and carboxylated single-walled carbon nanotubes were mainly favored by hydrophobic force [56]. The hydrophobic properties of the nanotube sidewall and those present in the BSA molecule likely cause non-covalent bonding allowing the nanotubes to be functionalized [75-80]. These hydrophobic forces and π-π stacking, caused by aromatic amino acids phenylalanine and tryptophan, alters the secondary structure of BSA [79]. This can be visualized through the intrinsic fluorescence of the tryptophan residues that, due to the opening of the BSA conformation, are exposed closer to the CNT, leading to a reduction in fluorescence [79,80]. The carboxyl functional group is also expected to contribute to stronger CNT-BSA interactions due to electrostatic and hydrogen bonding [80]. Simulation experiments between BSA and SWCNTs have shown that the optimum geometry and interaction configuration was determined by the size of the BSA binding pocket, and changes in dipole moment before and after interaction [80]. Measurements were taken using a Jasco FT/IR – 6200 Fourier Transform Infrared Spectrometer.

Samples were measured at a resolution of 4cm^{-1}, with 64 scans per test, and in range from 400 to 4000/cm^{-1}. [Figure 7] shows differences in FTIR spectra comparing [Figure 7. a], pristine single walled carbon nanotubes were dispersed in 1% sodium deoxycholate as previously described, BSA [Figure 7.b], and [Figure 7.c] SWCNT then dispersed with BSA.

As seen in [Figure 7. b], BSA is visualized spectrally with the amide groups, amide I and amide II, on the polypeptide with frequencies near 1650 cm^{-1} and 1540 cm^{-1} [75]. The largest evidence of successful bonding is the demonstration of these peaks to be present on the purified SWCNTs. Centrifugation over 20,000x g over 20 minutes is sufficient to remove BSA in the pellet of aggregated CNTs. The other determining factor to back up this assumption is the DLS data showing only one sharp peak as opposed to multiple.

The second important region for BSA/SWCNT interaction is the high frequency range from 2700-3600cm^{-1} [75]. Here, evidence of bonding is demonstrated by the broadening of the O-H around 3400cm^{-1}, indicating hydrogen bonding interactions ae taking place on the CNT surface. Changes in the secondary and tertiary structure due to interactions with the nanotube sidewall are confirmed by the decrease in intensity of the absorption bands in the high frequency region [75]. This is attributed to the vibration spectra of three complexes, Glycine:Glycine, Glutamic acid: threonine, and Aspartic acid: Lysine complexes account for hydrogen, ion-dipole, and ion-ion bonds [75].

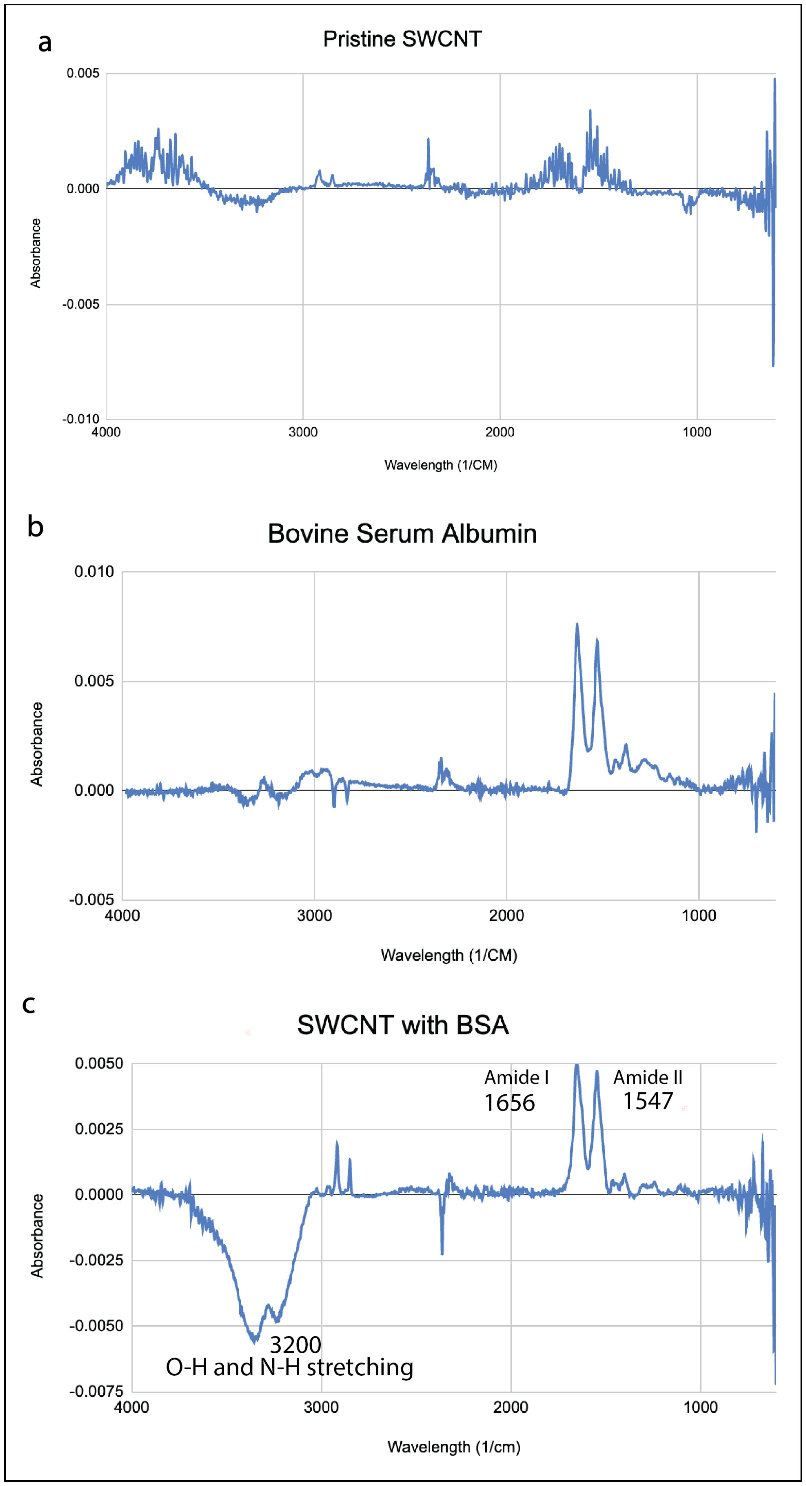

FIGURE 7 FTIR ANALYSIS. A) SWNT DISPERSION. B) BSA. C) CARBOXYLATED SWCNT DISPERSED WITH BSA.

4. Fibrin Collagen – Carbon Nanotube Hydrogels

There are two main strategies to form hybrid fibrin collagen hydrogels: the first being the impregnation of a collagen base pre-formed gel with fibrin, and the second being the constituents being mixed pre-polymerization, with the ladder forming much stronger protein interactions [45]. Differences in approaches to pre-polymerization mixtures have been taken including sequentially adding the constituents, medium, fibrinogen, sodium hydroxide, tropocollagen, thrombin at 4°C, then triggering polymerization at 37°C [45]. Another protocol mixes the two proteins, for example, the first mixture is tropocollagen and fibrinogen which is then mixed with a NaOH-thrombin solution. A third protocol neutralizes the collagen first before then adding thrombin and finally fibrinogen [45]. This strategy is more straightforward than the other two and lends itself better to the work being done here.

The method developed here was based off the established work done in the Black Lab's protocol (Ye, Kathy Yuan, et al. "Encapsulation of Cardiomyocytes in a Fibrin Hydrogel for Cardiac Tissue Engineering.") [81] and uses three solutions that when mixed, encapsulate cells within a fibrin hydrogel. In short, an "F" solution comprised of fibrinogen diluted to desired concentration with 20mM HEPES 0.9% saline buffer, a "T" solution, containing the appropriate thrombin concentration as well as CaCl2+ diluted in DMEM media, and a final cell solution, which is the isolated cardiomyocytes in culture media [81]. The measurements for each solution used a 4:1:1 ratio respectively [81]. Once prepared, the "T" solution is mixed with the cells, followed by the "F" solution, which once added polymerization begins immediately. The solution can then be injected into the mold of choice and is polymerized at 37°C for 20min. This protocol gives us cells encapsulated into a 3.3mg/ml fibrin hydrogel, and the framework for developing a hybrid hydrogel [81].

In preparation, fibrinogen from bovine plasma was purchased from Sigma-Aldrich [F8630]. Stock solution was prepared by slowly mixing with 20mM HEPES and saline buffer over sever hours at 37°C. The solution was left to settle overnight at 4°C. The following day the mixture was warmed to 37°C and strained and then sterile filtered (0.25 µm). The concentration was then quantified by taking the A280 with a NanoDrop. Final concentrations of ~55mg/ml were achieved, and the samples were stored at -80°C. Thrombin from bovine plasma was purchased from Sigma-Aldrich [T7513]. A stock solution was made with 0.9% saline in DI water, with an end concentration of 25U/ml. The stock was aliquoted and stored at -80C. Collagen I derived from rat tail was purchased from Corning [CB-40236].

The goal for this hydrogel formulation was to produce a 3.3mg/ml fibrin, 1mg/ml collagen hydrogel that could incorporate up to 0.5mg/ml SWCNT. This required changes to be made to the protein and media based "F" and "T" solution as the cell solution would not allow for modifications. The first step was to make new stock solutions high enough to reduce the volume initially needed, but not so high as to risk precipitation. Consistent stocks at a concentration of ~55mg/ml fibrinogen were able to be made. This would leave space for the collagen/DMEM mixture to be added. Polymerized by a change in pH, collagen would be mixed with DMEM 68% to collagen 30% followed by a 2-2.5% $NaHCO_3$ to be added dropwise. The collagen DMEM mixture would turn yellow, then gradually turn pink as HaHCO3 is added indicating the correct pH. The "T" and cell solution (DMEM) could be mixed, the collagen mixture prepared, then neutralized, immediately following color indicating the correct pH, the fibrinogen is added, then followed by the combined “T” and cell solution. All solutions can be prepared beforehand and combined in a matter of seconds, well mixed, then aliquoted into the desired mold.

To incorporate carbon nanotubes, the procedure would be the same, however room for the required concentration of SWCNTs would made by reducing the volume of DMEM added to the collagen. Being dispersed in the HEPES buffer system, the SWCNTs could be added into the mixture of proteins after the collagen pH hit the correct pH. All gels constituents were kept on ice until their immediate use. Following injection into the molds, gels were incubated at 37°C for 30-60 minutes before being removed from the mold and put into media. After consistent acellular hydrogels could be made, acellular characterization is required to define the properties and help elucidate future cellular response.

4.1 Acellular Characterization of Hydrogels

Hydrogel mechanical properties strongly influence cellular and tissue compatibility and performance. Before cells are tested, acellular characterization of the material is crucial for elucidating their effects on cells. Here, rheology and compression testing are used to highlight the difference in properties between each test condition and help draw conclusions when cells are introduced into the constructs. Three hydrogel test conditions were able to be formulated that would eventually be tested with cardiomyocytes. Condition 1, pristine fibrin collagen hydrogel with 3.3mg/ml fibrin, 1mg/ml collagen, condition 2, fibrin collagen with 0.1mg/ml CNT, and condition 3, fibrin collagen with 0.5mg/ml CNT. In all acellular gels used for characterization, DMEM media was used as a substitute for the cell solution. For rheological tests, fibrin will be tested as an additional condition to demonstrate the mechanical improvements of blended fibrin collagen hydrogels.

4.1.1 Rheology

Rheological characterization is a powerful tool for hydrogel characterization with its small sample size, ease of use, and sensitivity. The predominant method is small-amplitude oscillatory shear (SAOS), which generates shear flow by continuously oscillating the sample about its equilibrium position [58]. Polymer hydrogels are viscoelastic materials, and these measurements record the storage modulus (G’), representing the materials elastic energy, as well as loss modulus (G”) representing the materials viscous energy. The amplitude of oscillation represents the maximum stress or strain applied while the frequency represents the oscillations per second. Rheology can play an important role in elucidating cell responses to a biomaterial and is used to determine a materials viscoelastic region

Samples were loaded onto parallel 20mm Peletier plates, set to a gap height of 1000 µm. The linear viscoelastic region or LVR is the range of deformation the material can resist, beyond this limit in the non-linear regime the material will breakdown [83]. When forces are applied to the material outside these limits, measurements can no longer be associated with the material’s structural properties. The LVR can be elucidated experimentally by running stress or strain sweeps and observing when the sample begins to yield, corresponding to the point G’ becomes stress or strain dependent.

All testing was done on TA Rheometer HR20. Test geometry was 20mm Pelletier plates. Before The test begins, the plates are cooled to 4°C, this ensures all tests start from the same point. Hydrogels are prepared (on ice) and once mixed immediately pipetted onto the plates. A total sample volume for each gel was 300µl. The total height between the plates was 1000µm. Once gel was applied to the plate, the transducer was lowered slowly to the correct height, and the program would begin. The first step in every test was a programed temperature ramp from 4°C – 37°C. Each test was done with n=3 and results were averaged.

4.1.2 Gelation

The first property to determine when working with a new hydrogel formulation is the gelation or polymerization time. This is the duration required for the material to crosslink from liquid-like to a solid-like network through chemical or physical bonding, reaching a point where it exhibits stable mechanical properties able to resist flow under stress [82,83]. This metric is critical to start with as all subsequent tests must be performed on fully polymerized gels. Initial test parameters for strain amplitude (γ0) and frequency (ω0), should be referenced in the literature, or chosen arbitrarily to start [83].

Sourced from the literature, each condition was initially tested with a 5% strain rate at 1Hz [83]. Polymerization is monitored by observing the storage modulus (G') and loss modulus (G") as a function of time (t). As G' rises it becomes less viscous and more elastic until the polymer network is formed, shown on the graph as the plateau of G'. [Figure 8] shows the gelation of fibrin collagen, monitoring G' and G" as a function of time. This graph demonstrates how quickly the material transitions from liquid to solid like behavior. Where initially G" is higher, as crosslinking occurs, G’ rapidly increases until it crosses G” indicating gel behavior is more elastic. Because G” values are substantially smaller throughout all tests, storage modulus will be used as the primary measurement to show hydrogel behavior.

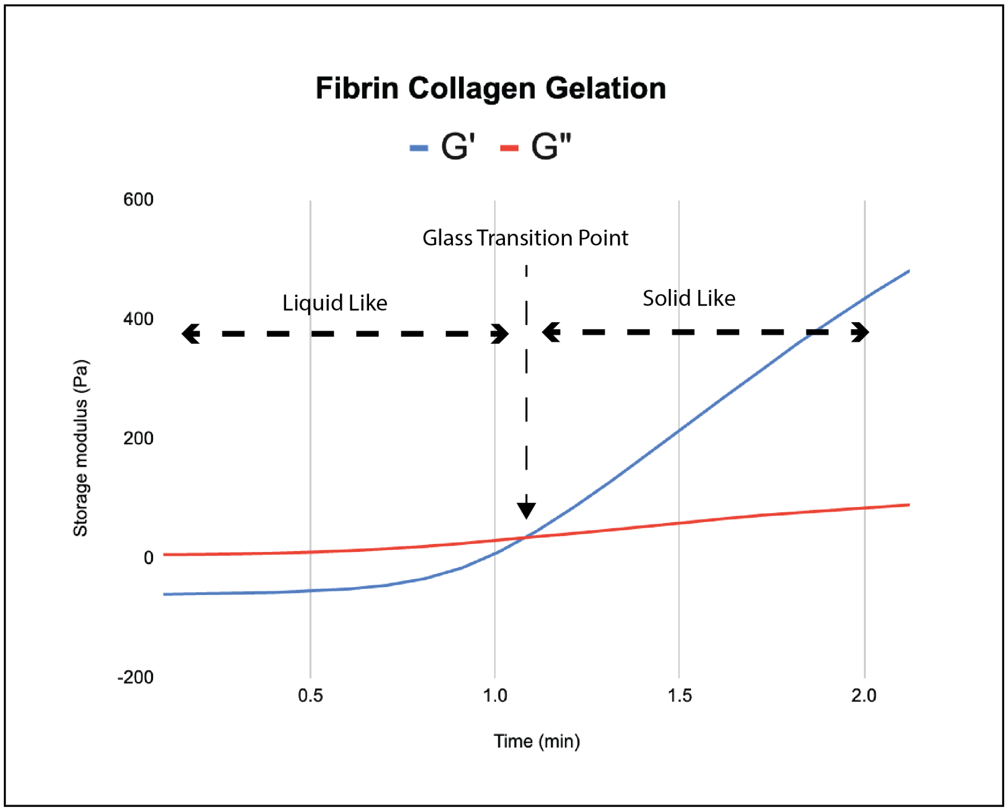

FIGURE 8 POLYMERIZATION GLASS TRANSITION POINT

As previously mentioned, the start point is immediately after the components are mixed and applied to the cooled rheometer plates. To observe polymerization kinetics, data is recorded immediately following the temperature ramp from 4-37°C. The end point of the test is when G’ equalizes and is seen as a plateau of mechanical properties.

Gelation time measured by the rheometer shows polymerization always occurring within roughly the first 15-20 minutes for fibrin and fibrin collagen samples, and 30-45+ minutes for samples incorporating SWCNTs [Figure 9.] and [Table 2]. While all formulations showed the transition from liquid to solid like behavior between ~1.5 - 3 minutes, the average time to form a fully polymerized gel changed as the formulation became more complex. In [Figure 9. a] we can see the rapid polymerization of fibrin. The fibrin matrix polymerizes so quickly, there is a sharp drop in G’ that occurs before the network becomes stable. This could be due to the fibers being too densely packed and the gel undergoes reorganization or rearmament, causing a drop in rigidity. When fibrin and collagen are mixed, we do not see this re-arrangement. With the increasing concentration of CNTs being incorporated into the matrix, the gelation time of the network increases drastically, however this is challenging to capture with the rheometer. This could be caused by the force being put on the sample by the rheometer during polymerization causing the nanomaterials to move as the matrix forms. Because of the time that it takes, evaporation occurs drying out the sample giving inaccurate data. When CNT incorporated gels that were polymerized in a mold for ~1hr before being removed they were always notably stiffer as SWCNT concentrations increased. This could be observed simply by manipulating them physically. This became apparent when trying to record data for 0.5mg/ml SWCNT gels. As seen in [Figure 9, d] G’ does plateau however then continues until the sample becomes unstable due to evaporation.

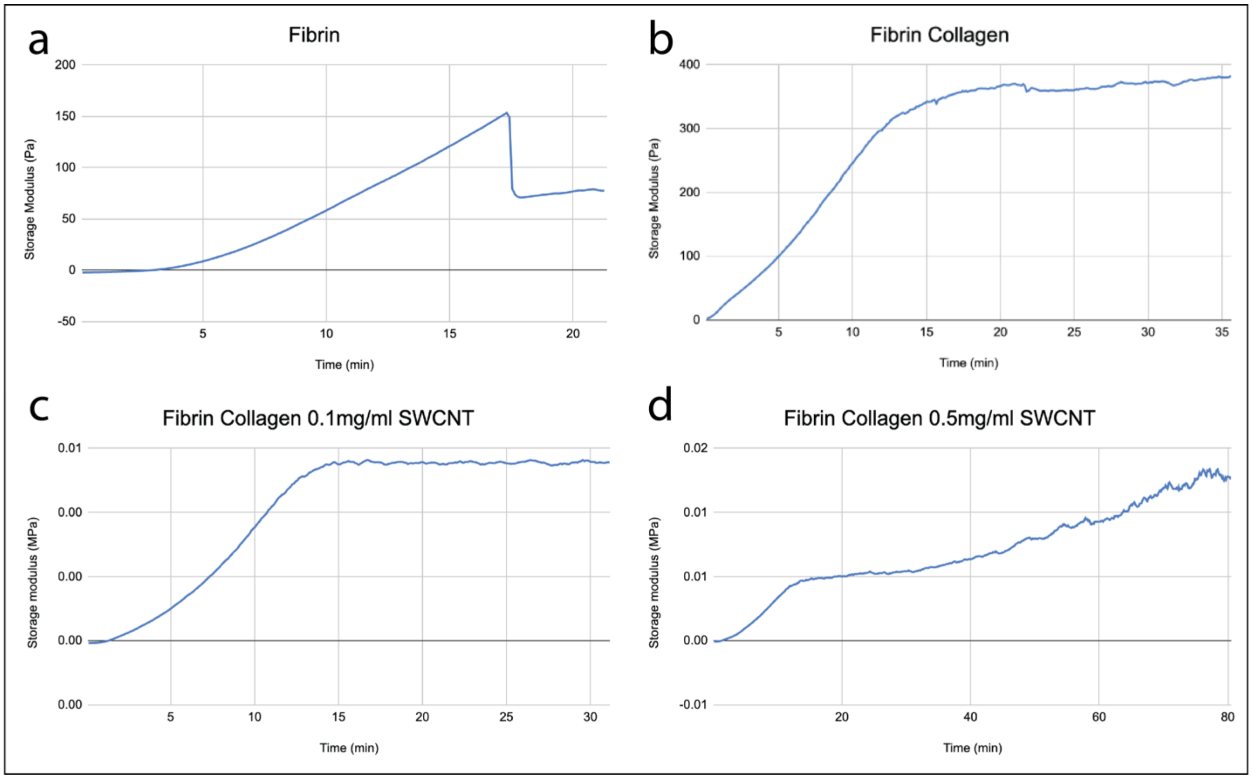

FIGURE 9 HYDROGEL POLYMERIZATION.

4.1.3 Strain Sweep

After polymerization times were determined, strain and frequency sweeps were then conducted to determine the LVR. For strain measurements, controlled deformation (strain) is applied, and the resulting stress is measured. The equation $\gamma(t) = \gamma0(\sin \omega t)$ represents the oscillatory shear strain applied to the sample while the equation $\tau(t) = \tau0(\sin \omega t + \delta)$ measures the response [82,83]. The phase difference of the phase shift between the applied strain and measured stress is measured. While elastic materials exhibiting only elastic-like behavior will have a phase perfectly in sync ($\delta = 0°$), purely viscous or liquid-like behavior has a phase shift of 90 ($\delta = 90°$), meaning the stress is a quarter cycle behind the applied strain [82,83].

Using previously determined gelation times [Table 2] ; strain sweeps were performed [Figure 10.]. After the initial temperature ramp, a soak time was programmed based on data from the previous test. The sweep increases strain from 0.1 to 100% strain. These tests were conducted with a frequency of ω0 = 1.0 Hz (6.3 rad s^{-1}) as an arbitrary number sourced from the literature. The LVR is the linear region of G', where the breaking point is where the graph goes non-linear [82,83]. As recorded in [Table 2], the fibrin and fibrin collagen results gave yield strains at 10 and 12.5% respectively which is consistent with the liter) measures the resulting stress. With CNT incorporated gels, the G' drops considerably from equilibrium, however, does not deviate from linear until 20% for 0.1mg/ml CNT and 22% for 0.5mg/ml CNT. As found from gelation data, the hydrogel networks became more complex by using mixing fibrin and collagen then adding CNTs. This is further shown by observing the phase angle for each formulation under the rheometer. The simpler networks of fibrin and collagen had lower phase angles 2-4 degrees, while CNT formulations had over 6 degrees. This could be an indication the data could be off if compared to gels that are polymerized in an incubator.

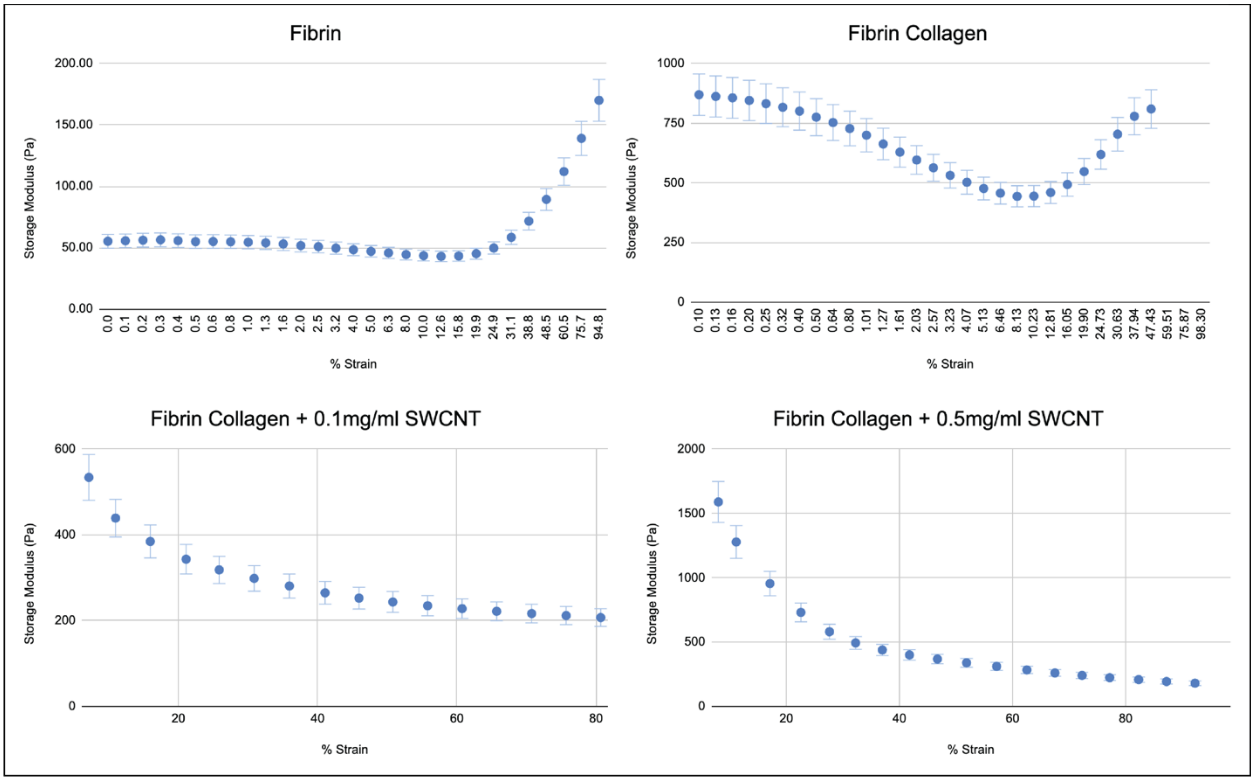

FIGURE 10 STRAIN SWEEP.

4.1.4 Frequency Sweep

For frequency sweeps, oscillatory strain and measure the materials response in terms of the complex moduli, which is described as G*(w) = s*/g* = G′ + iG″ with G′ and G″ as the real (elastic) and imaginary (viscous) components of G*, respectively [82,83]. Due to the dominance of G', it is used as the measurement to determine the relationship between G' and frequency. These sweeps were conducted from 0.01 to 100 Hz using the previously determined strain figures.

Demonstrating that the appropriate strain levels were determined in the previous tests, G' largely stayed consistent as the frequency was slowly increased until the breakdown of the matrix. Fibrin and fibrin collagen averaged 8-10Hz respectively which is consistent with the literature. Resistance increased with CNT concentration as 0.1mg/ml CNTs limit was 12Hz and 0.5mg/ml 17Hz. Tan δ or loss factor measured as tan δ = G"/G' gives insight to the balance between the two within the material. By monitoring tan(δ) it could be confirmed when the hydrogel network broke down as a large shift occurred consistent with the G' becoming non-linear. As seen in [Table 2], limits of fibrin and fibrin collagen were similar around 8 and 10 Hz respectively. While 0.1 and 0.5 mg/ml CNT were consistent with an increase to 12 and 17 Hz respectively. After the strain and amplitude figures for each gel are found, all future rheological testing can be performed within the hydrogel LVR.

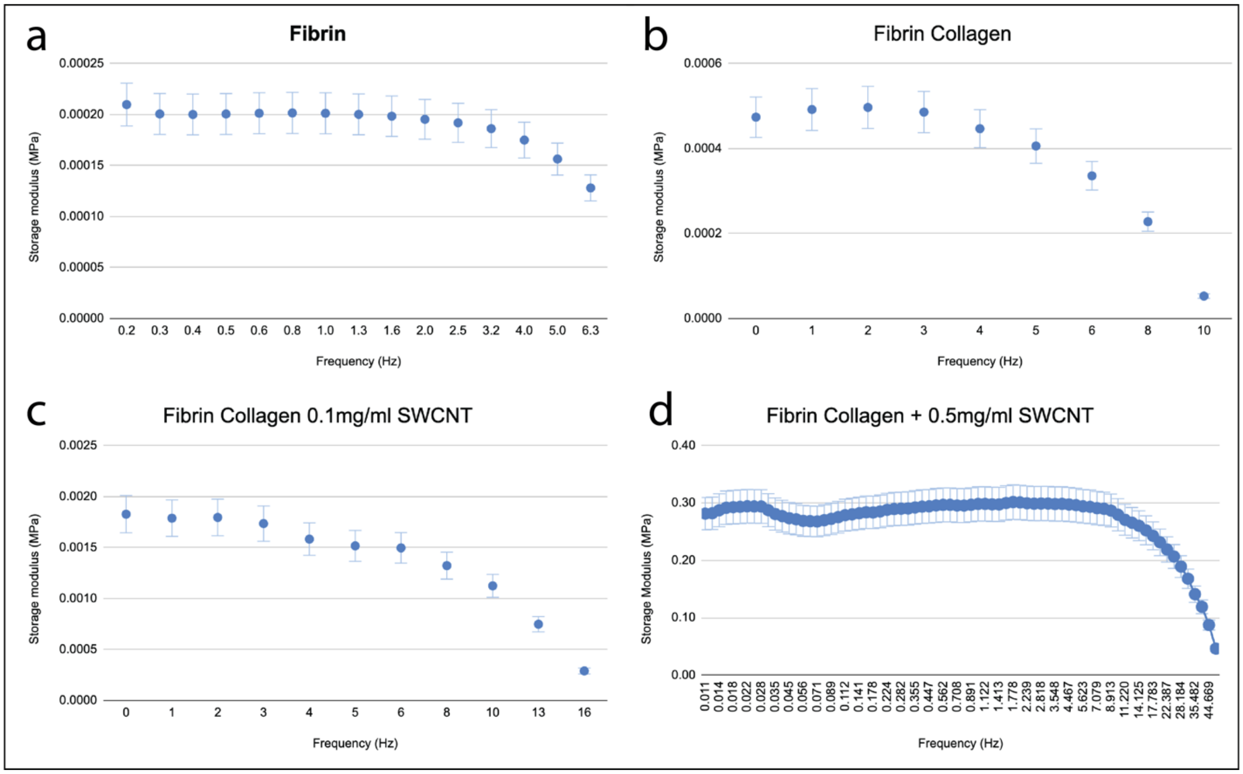

FIGURE 11 FREQUENCY SWEEP.

4.1.5. Time Sweeps

A final time sweep using the found polymerization time, strain and frequency sweeps is then conducted to determine a final storage modulus result. [Figure 11] demonstrates each of the four conditions at equilibrium over the course of a twenty-minute test. This test highlights the differences in elastic behavior for each condition. Fibrin averaged 154 Pa, fibrin collagen 465 Pa, 0.1mg/ml SWCNT 2255 Pa, and 0.5mg/ml 4034 Pa.

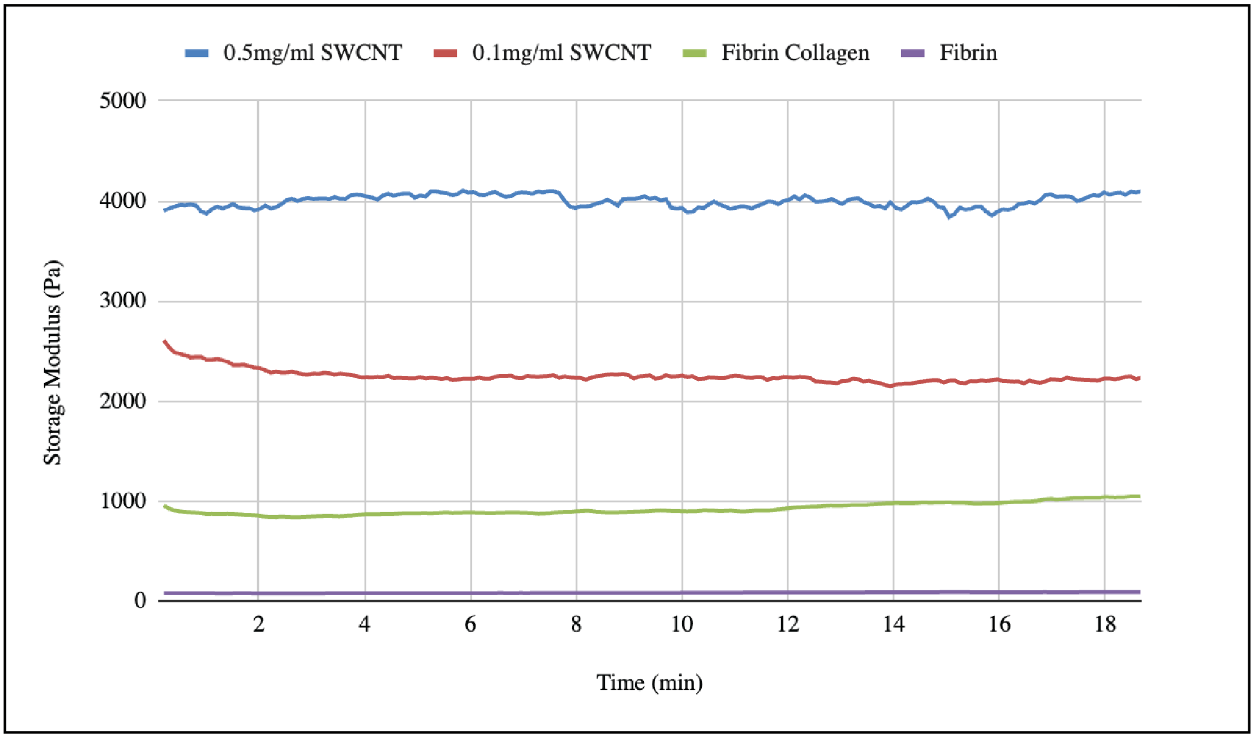

FIGURE 12. FINAL TIME SWEEP

4.1.6. Rheology Results

The rheological characterization tests are summarized in [Table 2]. First, it was demonstrated that collagen was able to enhance the mechanical properties of fibrin by creating a hybrid network. The polymerization time increases slightly due to the increased complexity of the system, however once equilibrium is reached, there are consistent performance advantages to the hybrid hydrogels. The interpenetrating polymer networks expand the LVR from 10-12.5% strain, 8-10Hz in frequency, and the overall elasticity demonstrated by G’ from 154 Pa to 465 Pa. As expected, when carbon nanotubes are introduced, further increases in performance were shown as a function of concentration. The LVR was further extended with 0.1 & 0.5mg/ml SWCNT samples extending the strain to 20% and 22% respectably and the amplitude to 12Hz and 17Hz respectably. The contributions here resulted in a massive overall increase in elasticity to 2.2kPa and over 4kPa.

TABLE 2: RHEOLOGY

	Gelation (min)	**Strain %**	**Frequency (Hz)**	**G’ (Pa)**	**Phase angle °**	**tan(δ)**
Fibrin	15	10	8	154	2.3	0.15
Fibrin Collagen	20	12.5	10	465	4	0.09
0.1 mg/ml SWCNT	30	20	12	2255	6	0.2
0.5 mg/ml SWCNT	45+	22	17	4034	x	x

4.1.7. Dynamic Mechanical Analysis: Compression

Dynamic Mechanical Analysis to determine Young's modulus of hydrogels of acellular hydrogels. The compressive modulus is an important indicator for a hydrogels ability to accommodate compressive strain during cardiac beating as well as influencing cellular developmental pathways. Cylindrical gels were prepared with dimensions were 14cm in diameter and 9cm in height and were chosen to achieve a 5:1 ratio which is suggested for compression testing based on literature. The three test conditions were pipetted into custom molds and set to polymerize for 1hour at 37C in an incubator. Gels were then plunged out of molds into 20mM HEPES buffer and incubated for 24 hours.

Measurements were taken with a TA Instruments Discovery DMA 850. Samples were applied to the parallel plates, and excess water was removed. A preload was set to 0.03N was used after it was experimentally determined to give stress strain curves with no artifacts or errors. Samples were compressed to a strain at a rate of 16um/s, which was also experimentally determined. Calculates were done on the linear portion (typically ~4-6%) of the stress strain curve [n=3], were calculated and averaged for each condition.

TABLE 3: COMPRESSION DATA

Condition	**Young's Modulus (kPa)** ***E***
Pristine	10.4
0.1mg/ml CNT	14.7
0.5 mg/ml CNT	21.61

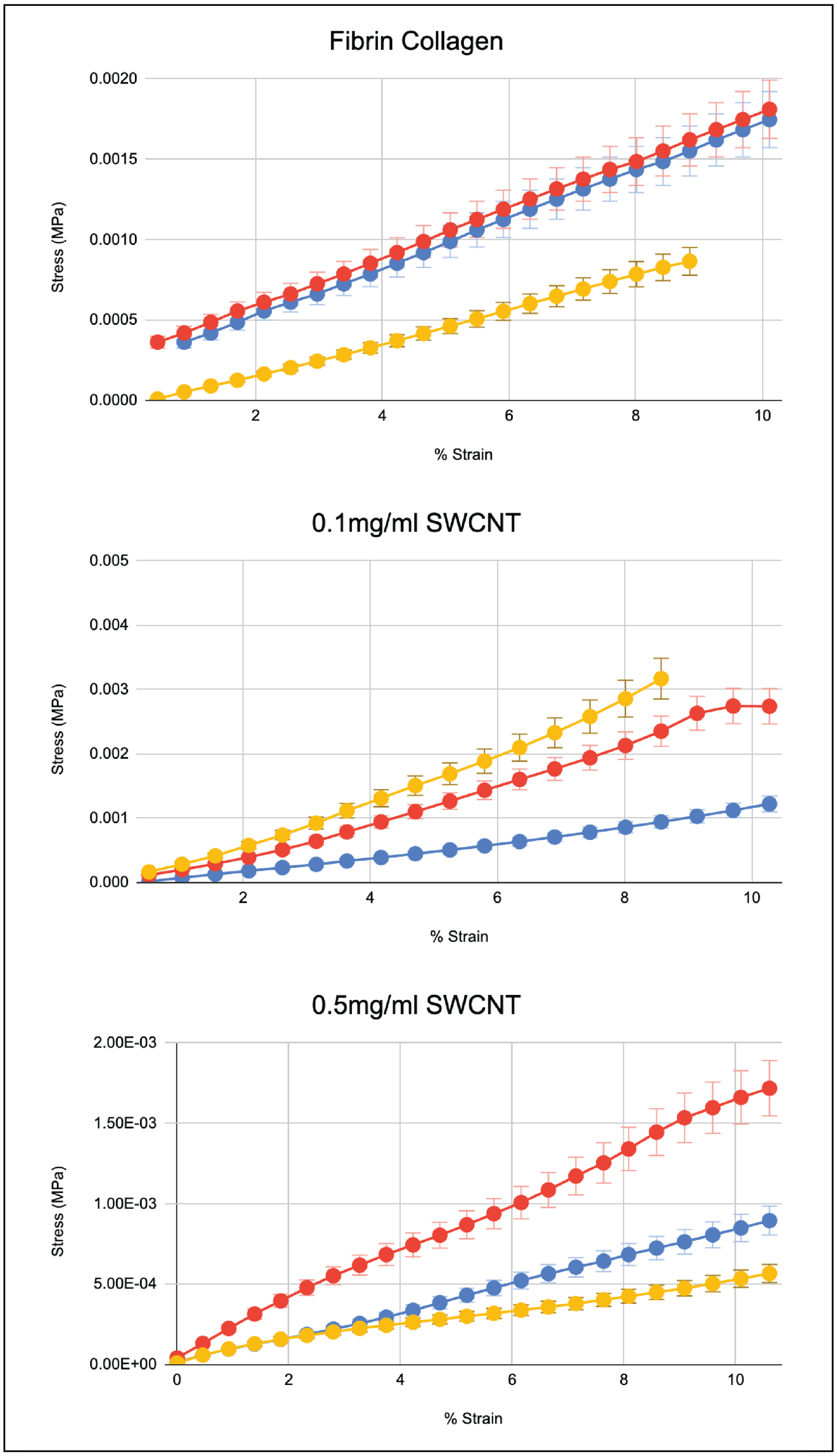

FIGURE 13. DYNAMIC MECHANICAL ANALYSIS.

As expected, the introduction of SWCNTs significantly improved the compressive strength and resilience of the hydrogels increasing the Young's modulus from 10.4 kPa to over 20kPa, like rat right ventricular myocardium (20 – 54 kPa) [64]. Due to the intrinsic stiffness of the SWCNTs, when integrated into the hydrogel network they can distribute compressive load and resist deformation, maintaining.

4.1.8. Impedance Measurements

Hydrogels with SWCNTs homogenously incorporated into the matrix, aligned or not, are known to reduce electrical impedance as concentrations of nanotube increase. The electrical behavior of biphasic nanocomposite hydrogels will vary depending on the nanomaterials structure, synthesis method, and dispersion method. Carbon nanotube hydrogels have three different phases with distinct properties. The fibrin / collagen polymers acting as the insulating matrix, the nanotubes acting as the conductor, and the liquid phase representing water and the ions in the buffer system being used. Several methods are mentioned in the literature on evaluating electrical properties of pristine and composite hydrogels such as conductivity meters, 4-point probe, etc, with impedance spectroscopy is the most widely used [84].

Using the TA Rheomoeter, an Agilent 4284A LCR meter was used to measure the impedance for all test conditions. Hydrogels were prepared as previously mentioned; polymerized in molds and incubated for 24hrs before testing. Geometry of gels as tested was a 4mm cross sectional area with an average height of 0.5mm. Using an LCR meter, an AC current was applied over the range of frequencies 20 Hz – 100,000 Hz. [Figure 14,a] shows that for all frequencies, it was an increase in carbon nanotube content, decreased the impedance making the hydrogels more electrically conductive.

For all samples the impedance magnitude (|Z|) decreases as the frequency increases, becoming independent of frequency over 1 kHz. Consistent with the literature, as CNT concentration increases, impedance magnitude decreases.

[Figure 14.b] bode phase plot shows how each hydrogels impedance phase angle changes with frequency, reflecting how quickly the material is responding to alternating current. In all samples the phase starts around -70 degrees. Here, the zero phase crossing where phase angle changes from negative to positive makers a transition in the hydrogel's electrical behavior. As the phase angle becomes positive it begins to exhibit inductive like behavior. The 0.1mg/ml SWCNT sample makes the fastest and steepest transition indicating better charge transport and quicker electrical responsiveness. The 0.5mg/ml makes the second and pristine fibrin collagen is last. Due to material limitations this experiment was only performed with an n=1, and all data had to be entered by hand. Because of this, the difference could be due to an unseen change in water retention, or improper mixing of hydrogel constituents during assembly.

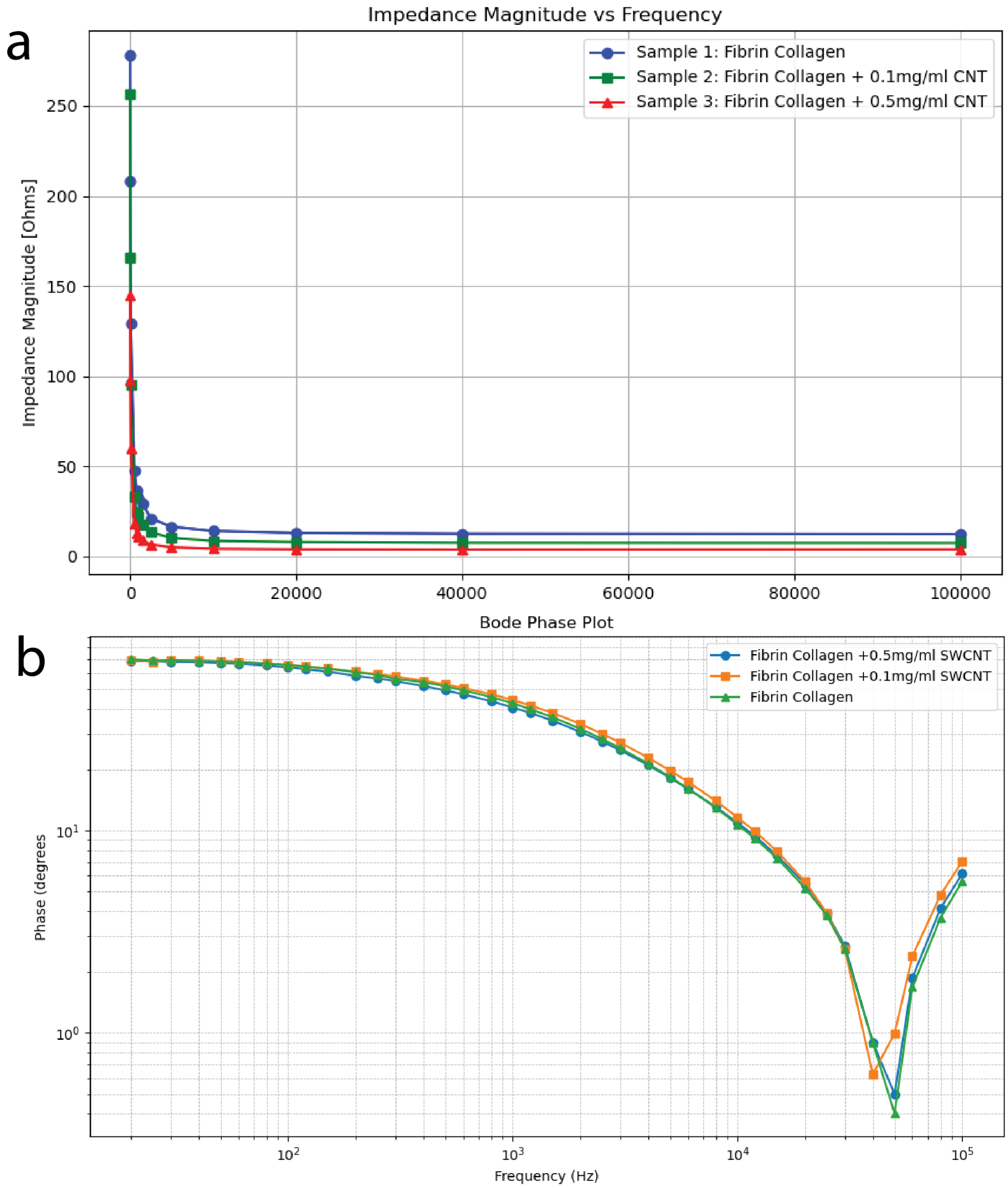

FIGURE 14. IMPEDANCE MEASUREMENTS. A) IMPEDANCE MAGINTUDE PLOT. B) BODE PHASE PLOT.

5. Cardiomyocyte Maturation

In vivo, maturation is the final phase of heart development when the organ becomes strong enough to function throughout its lifetime [85]. Cell structure, gene expression, metabolism, and other specialized functions are important characterizations of the change from fetal-like to adult cardiomyocytes. Before birth, the basic structure of the heart forms into a four chambered fetal heart [85]. After birth, cardiomyocytes further mature developing cytoskeletal structure and metabolism. There is a decrease in proliferation and within the first week most cells have completed their final cell division after which, the heart then increases in size through hypertrophy [85]. Key aspects of in vitro maturation strategies are considering morphology, electrophysiology, calcium handling, and metabolism.

In cardiomyocytes specifically, morphology is critical not only for providing basic structural framework but creating the necessary electrophysiological and contractile properties the organ demands. Membrane capacitance is directly proportional to the cells surface area, therefore when cells are smaller, they leave slower impulse propagation velocity and a smaller action potential upstroke velocity [22,85]. *In vivo,* adult cardiomyocytes are rod-shaped, anisotropic, roughly 150µm in length, 20 µm in width, 15 µm in height, and 40,000 µm^3 in volume. By contrast cultured hPSC-CMNs range from circular, to oblong shape, 30 µm in length, 10 µm in width, and a volume of 2000 µm^3 after a period in culture [22]. The natural elongated anisotropic shape gives the cell a high length to width ratio giving rise to long myofibrils and increasing cardiac contractility efficiency [22]. Because of these necessities, the difference between mature and immature morphology has a large impact on cell functionality.

Electrophysiology and action potential propagation are also crucial components of development. While adult cardiomyocytes are quiescent and don't depolarize unless triggered, immature cells will beat spontaneously [22]. This automaticity is controlled through the development of ion channels. The difference in action potential generated from immature vs mature cells is very different. Immature hPSC-CMs are less hyperpolarized around -60mV, while mature are around -90mV [22]. Immature cells demonstrate lower expression of the inward-rectifier potassium channel $K_{ir}2.1$, encoded by KCNJ2, which regulates the displacement of calcium out of the cell. In addition, the expression of fetal isoform $Na_v1.5$ α-subunit of the sodium channel encoded by SCN5A, leads to slower kinetics of channel activation and therefor a slower upstroke velocity on the action potential [22].

As previously mentioned, calcium handling plays crucial role sin contraction, signaling, metabolism, and transcriptional regulation [22]. Immature cells have poorly developed calcium dynamics, the lack of T-tubules delays calcium-induced calcium release due to spatial uncoupling of the LTCCs and RYRs [22]. Over the course of maturation, calcium in the SR increase, as well as calcium cycling and dynamics, and T-tubual development [22].

Differences in metabolism are also dramatically different as fetal cells must utilize anaerobic glycolysis as the primary source of ATP due to low levels of fatty acids and high levels of lactate [22]. As development continues, higher oxygen content and an increase in dietary lipids mediate metabolomic reprogramming, resulting in 80% of adult cells total energy coming from the B-oxidation of fatty acids [22, 85].

These characteristics highlight the importance of cell behavior analysis through cell culture. Many models are used to investigate heart development including mice, rat, chick, and human embryos, while the species vary, the underlying processes and regulatory singles are similar.

5.1 Cell Culture

The hearts of 2–3-day old neonatal rat pups were harvested and digested in collagenase, isolating the cardiomyocytes from the ECM. After the isolation steps were complete, the cells were resuspended in DMEM, counted, and ready for use. Three testing conditions, pristine, 0.1mg/ml CNT, and 0.5mg/ml CNT were prepared to be tested for cytotoxicity and immunofluorescence. Each condition had an n=6 for both cytotoxicity and immunofluorescence. Neonatal rat cardiomyocytes were seeded at 1 million cells / ml and encapsulated in the hydrogels.

The gels were pipetted into molds [Figure 15] and incubated for 1hr. They were then plunged from the molds into cardiomyocyte media. Media constituted horse serum, 2% fetal bovine serum, 1% penicillin-streptomycin, 6 mg/mL -aminocaproic acid into DMEM, 50 μg/ml of ascorbic acid and 2 μg/ml of insulin in 25 μM HEPES. Cells were fed once a day for the entirety of their time in culture over the course of two weeks (14 days).

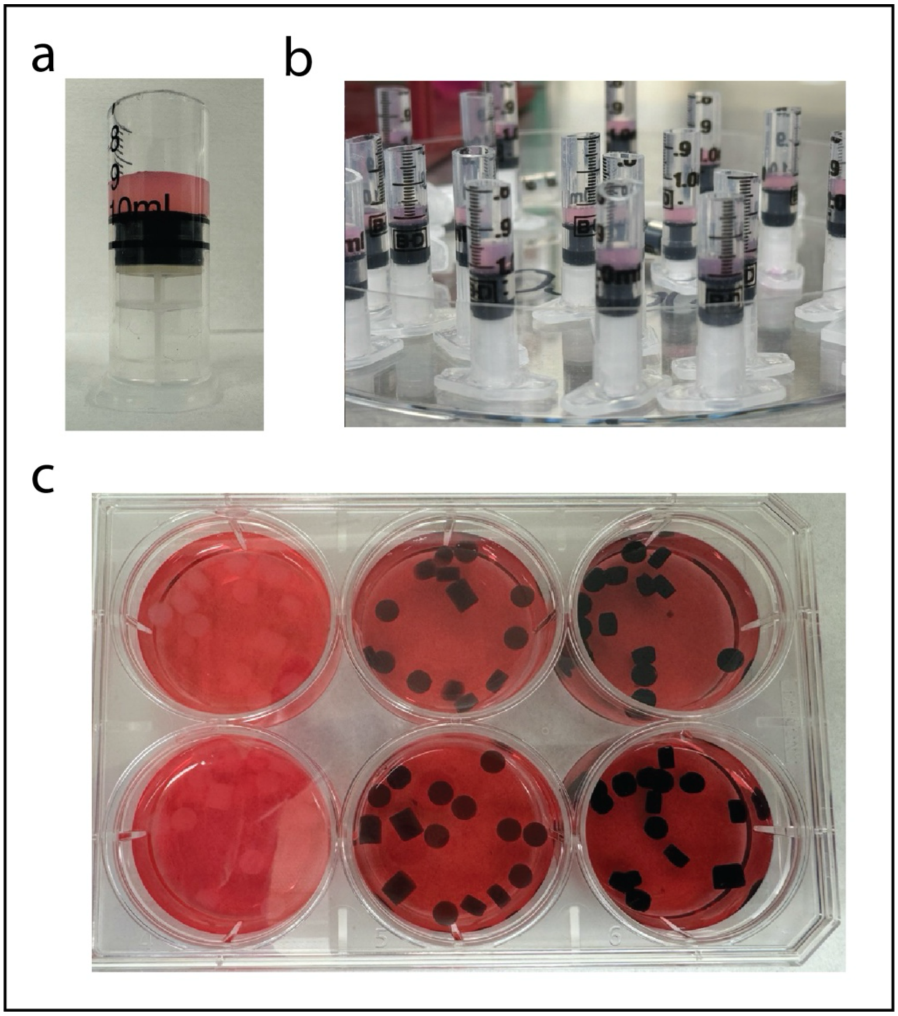

FIGURE 15. HYDROGELS. A & B) HYDROGELS POLYMERIZED IN MOLDS. C) FULLY FORMED HYDROGELS IN MEDIA.

5.2. Cytotoxicity Testing

Biocompatibility one of the most important aspects of cardiac tissue engineering as all downstream applications hinge on the seamless integration of the biomaterial with the native cardiac tissue. For nanomaterials, cytotoxicity is especially important and complex due to the extreme behavioral differences they are known to exhibit compared to their bulk counterparts. The toxicity of a material or substance refers to the amount it takes to kill an organism [86]. At the cellular level, cytotoxicity is measured by the amount of apoptosis or necrosis that occurs. Overall carbon nanotubes and other carbon-based materials are extremely attractive due to their nanoscale properties; however, it has been demonstrated that their interactions with organisms can be highly toxic [86]. As previously mentioned, factors such as dispersion quality, functionalization, as well as size, shape, surface area, lattice structure, surface charge, and aggregation state all influence their interactions with biological systems and toxicity [86].

For cytotoxicity testing, a "LIVE/DEAD™ Viability/Cytotoxicity Kit, for mammalian cells" was purchased from Invitrogen. Samples were rinsed 3x for 5 minutes each in PBS. From the kit, a 2mM EthD-1 solution and 4mM calcein-AM stock solutions were made and the appropriate amount added to the samples in PBS. The samples were covered and incubated for 30 minutes at room temperature before the dyes were removed and replaced with PBS. Samples were then viewed and imaged under a fluorescent microscope where the green fluorescence calcein-AM is excited by 494nm light and emits 517nm light and the red fluorescent ethidium homodimer-1 by 538nm light and emits 617 nm light.

While most of the cell culture was successful, on the day of imaging condition 3 (0.5mg/ml CNT) was contaminated and not able to be imaged. Additionally, time constraints only aloud for several images to be obtained on the fluorescent microscope. Therefore, meaningful results were not able to be obtained, and the experiment would have to be repeated. The three samples for condition 1 (pristine) that were imaged all showed a high levels of cell viability demonstrated by the green (live cells) fluorescent intensity, as well as z-stack imaging of red (dead cells) fluorescing throughout the constructs. For condition 2 (0.1mg/ml CNT), the same z-stacks were not able to be obtained, however the combined imaging shows the constructs appear to be largely viable. Due to contamination and lack of imaging time, these experiments will have to be repeated to obtain meaningful results.

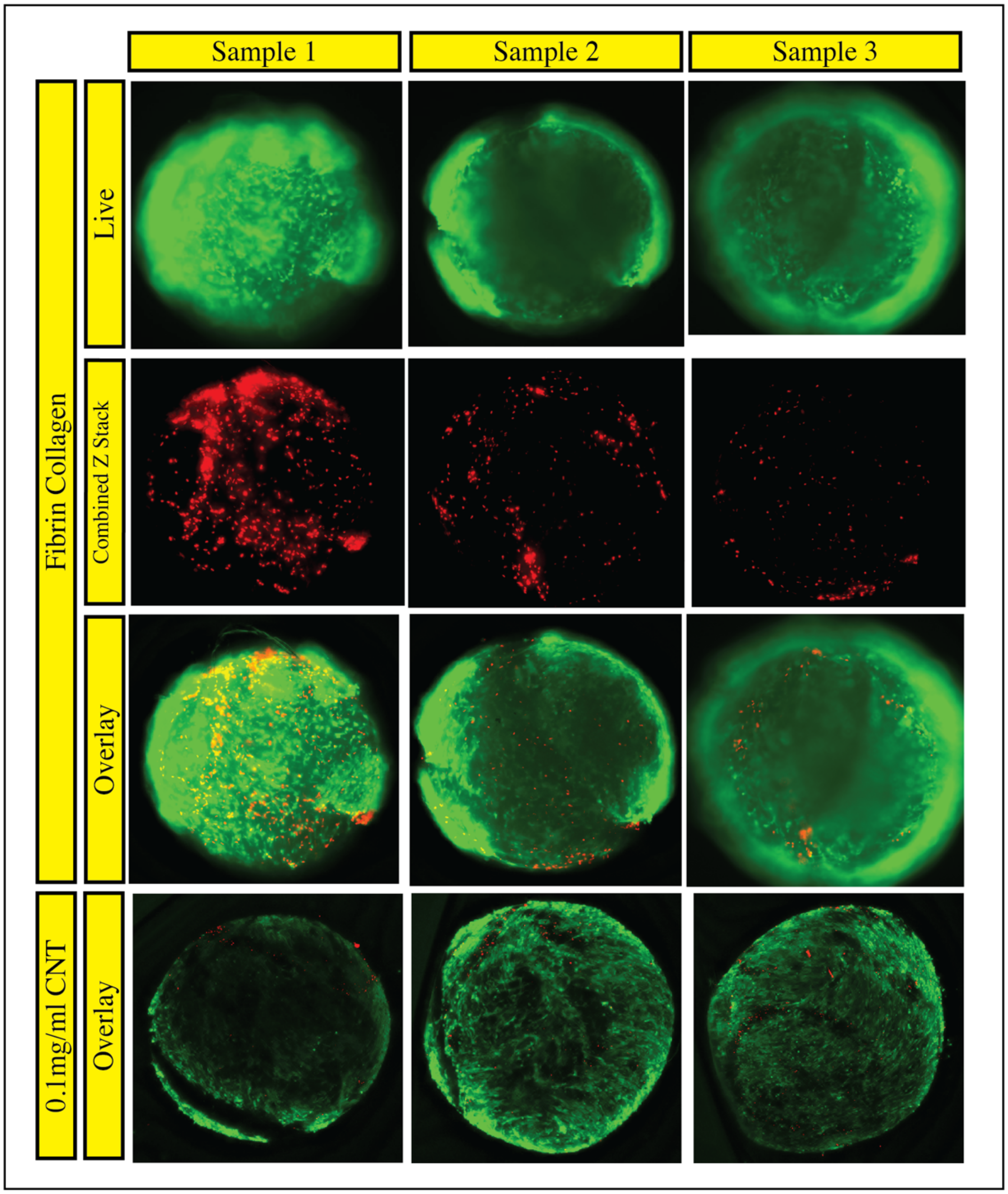

FIGURE 16. FLUORESCENT MICROSCOPIC IMAGING OF LIVE/DEAD STAINING.

5.3. Immunohistochemistry

Immunostaining is a crucial technique in cardiac research to visualize and analyze the expression of specific cardiac proteins and markers in efforts to establish differences in testing conditions. As previously stated, Cx43 is an important gap junction protein, and the pain protein in ventricular cardiomyocytes. Because of its roll in coupling, and therefore synchronized contraction, staining helps assess cell-cell communication, coupling / junction integrity, and proper location i.e intercalated discs. Alpha-actinin or a-actinin is a cytoskeletal protein found within the sarcomere Z-discs. Functionally this protein is an important component of the contractile apparatus. Staining for α-actinin is used to determine important morphological components of sarcomere organization to assess structure, alignment, and infer level of maturation. These two proteins were chosen to give insight into both functional intercellular communication as well as a representation of cardiomyocyte structure.

Samples are first washed 3 times for 5 minutes in PBS. They are then fixed with 4% paraformaldehyde in PBS for 3 hours at 4°C. They are then washed again in PBS before incubating in 0.1% Triton-X in PBS for half an hour to permeabilize the cell membranes. The Triton is then washed with another 3 PBS rinses for 10 minutes each. Before stained the samples are then blocked in 5% donkey serum in PBS for an hour and a half to prevent non-specific binding.

Two proteins were stained to evaluate expression, a-actinin and Connexin 43. Anti-Sarcomeric Alpha Actinin antibody [ab137346] rabbit polyclonal antibody was purchased from Abcam and used at a 1:50 dilution per manufacturer recommendation and visualized with Alexa Fluor® 488

AffiniPure™ Donkey Anti-Rabbit IgG (H+L) purchased from JacksonImmuno in red fluorescence. Connexin 43 Antibody [#3512] (rabbit) was purchased from Cell Signaling Inc. and used at a 1:100 dilution per manufacture recommendation. Alexa Fluor® 488 AffiniPure™ Donkey Anti-Rabbit IgG (H+L) was used to visualize in green fluorescence. Samples were incubated with stain for 3 – 4 hours and then rinsed with PBS. Before imaging samples Hoechst 33258 solution from Sigma-Aldrich was used to stain the cell nucleus in blue.

As with cytotoxicity testing, an n=6 was used for each sample condition. While there was no contamination in any samples, time only permitted imaging two samples for each condition. Because of this, meaningful results were not able to be obtained however analysis shown in [Fig.13] shows that it is possible that an increase in CNT concentration led to greater expression of Cx43 and a-actinin. With data showing the increased Young's modulus and electrical conductivity of hydrogels as CNT concentration increased this would be consistent with the literature. It has been demonstration that CNTs can promote development of gap junction and adherens junction proteins in infarcted regions [5.5]. Cardiomyocytes in culture also have been shown to demonstrate better alignment and elongation, notably with the upregulation of cardiac specific markers for sarcomeric α-actinin and Troponin I [5.6].

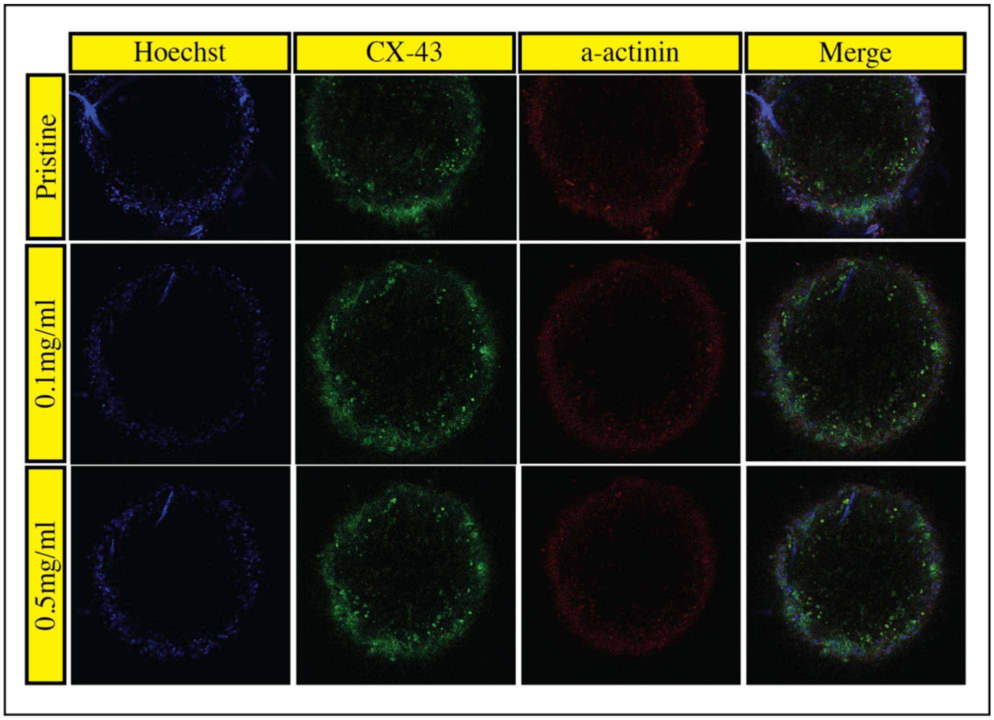

FIGURE 17. CONFOCAL MICROSCOPY IMAGING OF IMMUNOSTAIND CONSTRUCTS (10X)

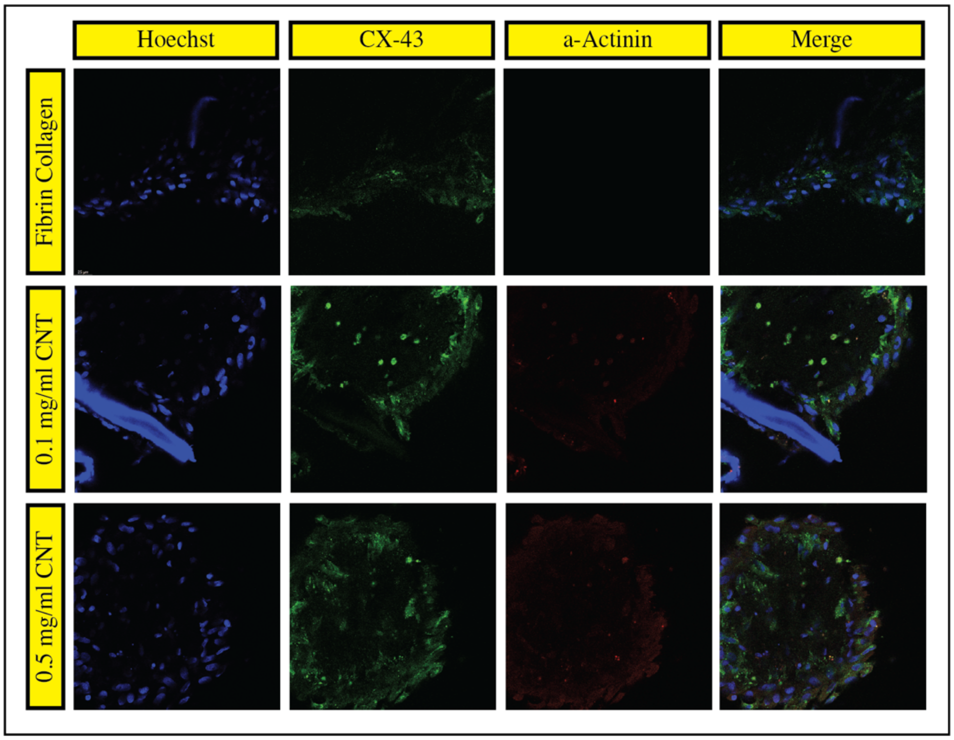

FIGURE 18. CONFOCAL MICROSCOPY IMAGING OF IMMUNOSTAIND CONSTRUCTS (40X)

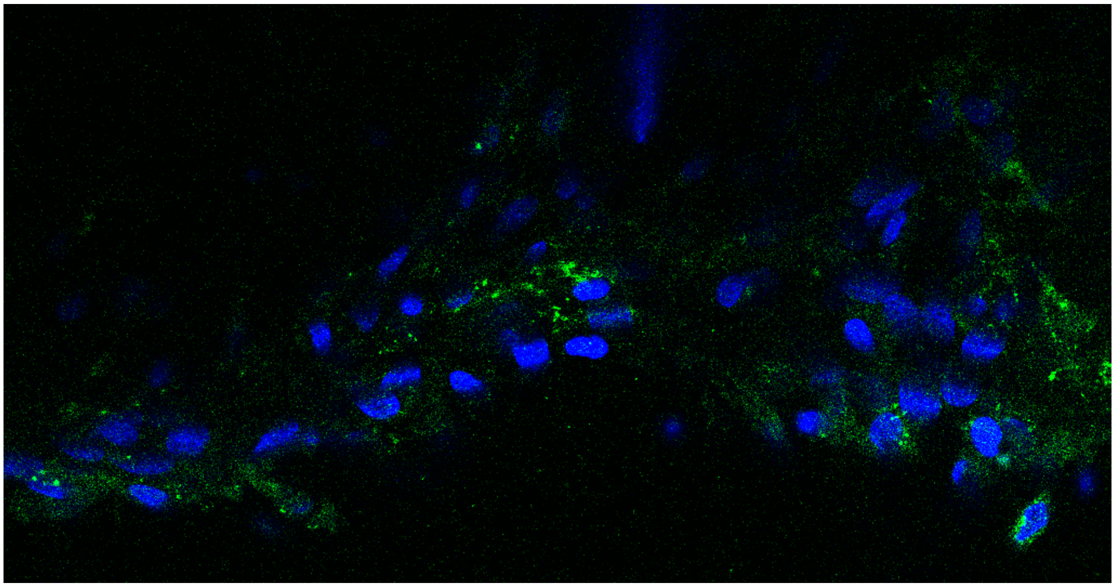

FIGURE 19. HIGH-RESOLUTION IMAGE, FIBRIN COLLAGEN.

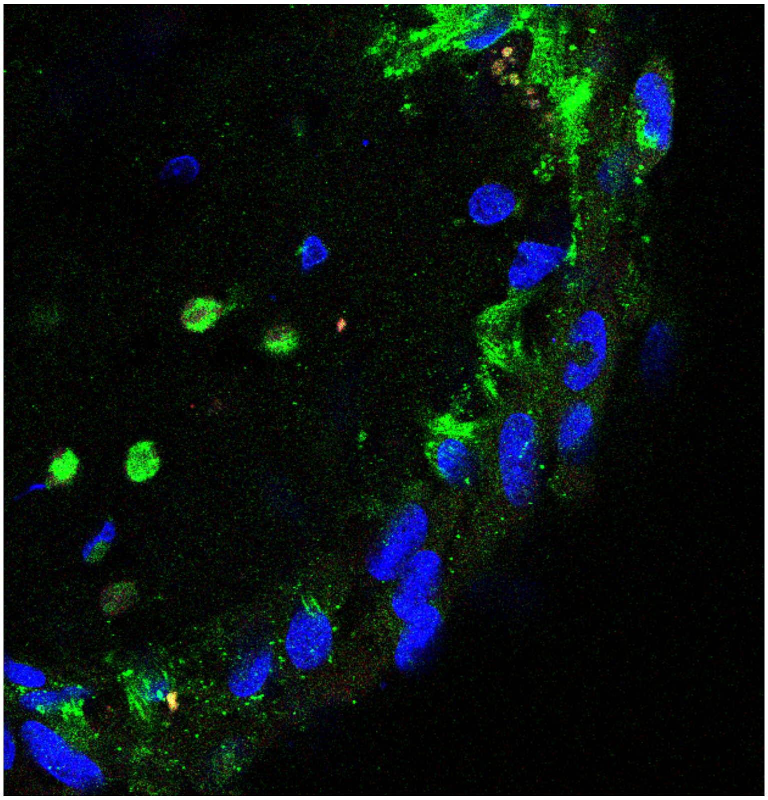

FIGURE 20 HIGH-RESOLUTION IMAGE, FIBRIN COLLAGEN 0.1MG/ML – SWCNT.

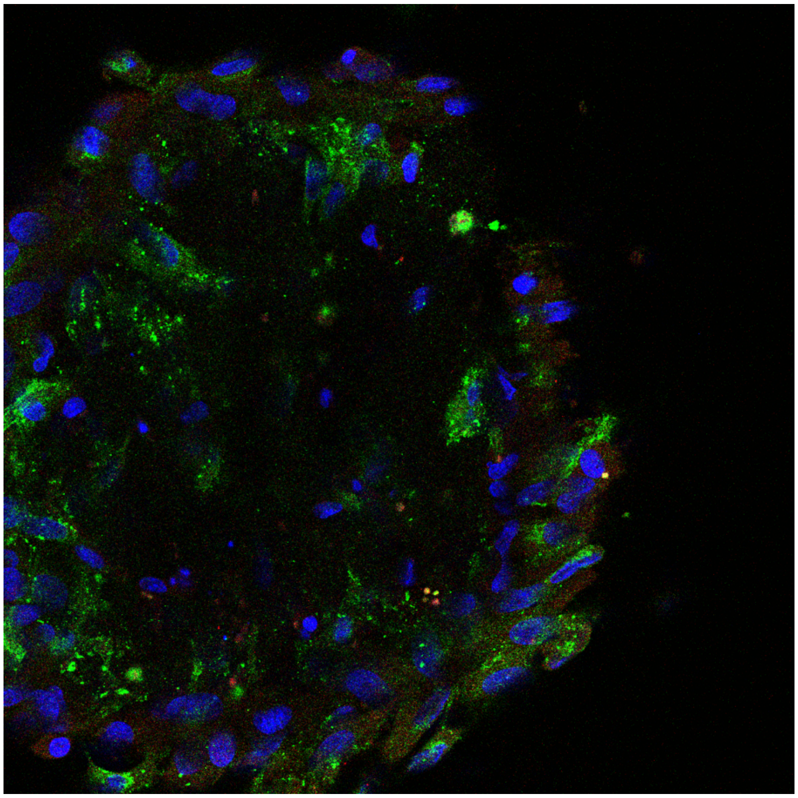

FIGURE 21. HIGH-RESOLUTION IMAGE, FIBRIN COLLAGEN – 0.5MG/ML SWCNT

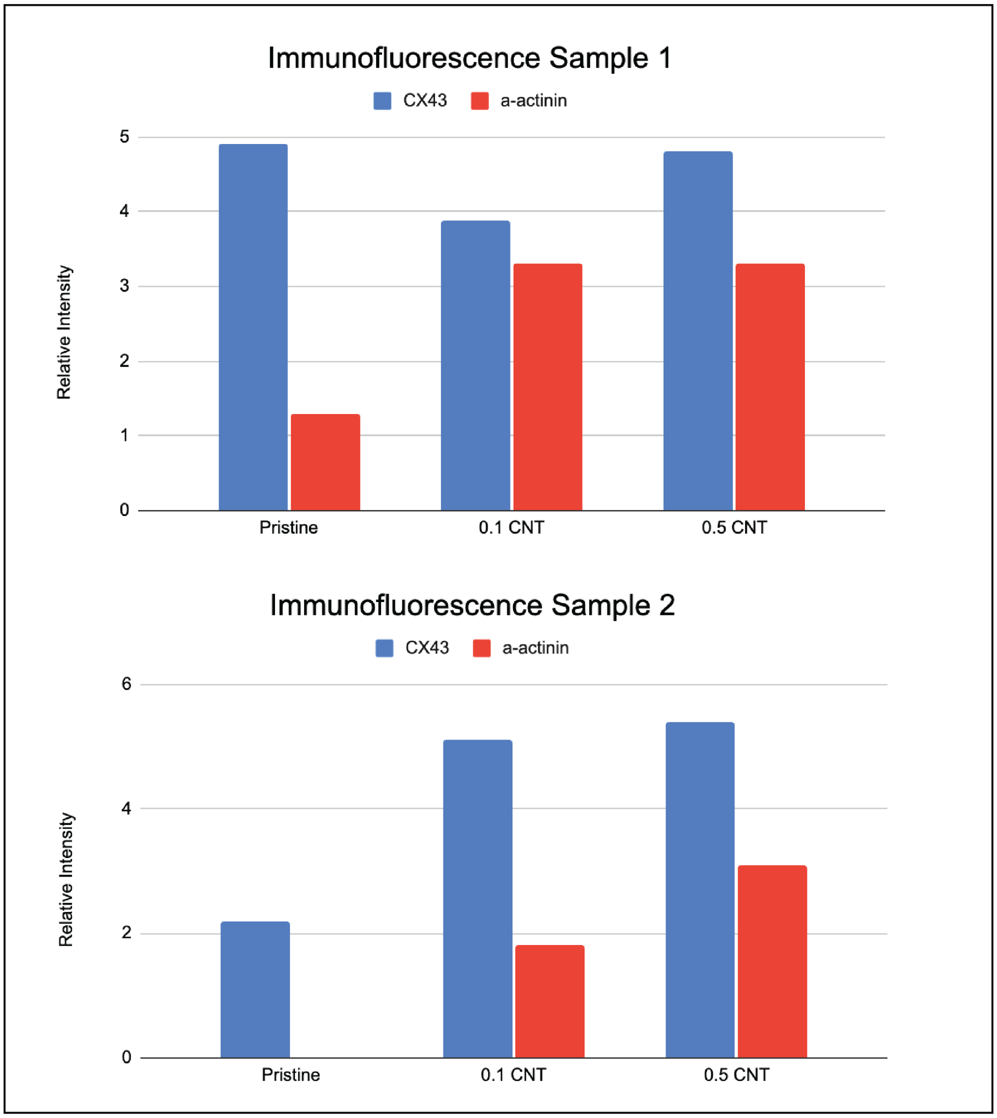

FIGURE 22. QUANTIFICATION OF PROTEIN EXPRESSION.

6. Conclusions

This work demonstrated the successful incorporation of carbon nanotubes into fibrin collagen biopolymer hydrogels, and the successful culture of neonatal rat cardiomyocytes therein. A combination of bile salt sodium deoxycholate, and BSA proved to be an effective method to disperse carboxylated single walled carbon nanotubes into 20mM HEPES + 0.9% saline buffer and analytical characterization methods were used to assess their physical, chemical, and colloidal properties. Dynamic light scattering was able to confirm a monodisperse homogenous sample of exfoliated carbon nanotubes, confirming the lack of aggregates and other impurities. FTIR was able to identify the non-covalent attachment of BSA onto the SWCNT sidewall through functional groups, and Zeta analysis confirmed the stability of the sample through evaluation of surface charge. All together demonstrating a stable carbon nanotube dispersion ready for use in biological systems.

Quantification Mechanical characterization of acellular constructs through rheology and compression testing demonstrated the increased physical stability of carbon nanotube incorporated hydrogels. Rheological techniques demonstrated that the combination of fibrin and collagen offered initial stability in terms of elasticity and resistance to strain. These properties were further enhanced by the addition of carbon nanotubes. As the concentration of carbon nanotubes was increased in the hydrogels, the storage modulus and compressive modulus both increased. To assess the enhanced electrical properties, impedance measurements were conducted across a range of frequencies. Increasing carbon nanotube concentrations led to a reduction in impedance at all frequencies, indicating improved electrical conductivity of the hydrogels. These acellular characterization techniques show that carbon nanotubes enhance both mechanical and electrical of fibrin collagen hydrogels.

Finally, 3D cell culture of neonatal rat cardiomyocytes was done to demonstrate the ability of these constructs to support live cells. While specific conclusions could not be drawn due to experimental constraints, these experiments can be considered a proof of concept for these hydrogels. The cytotoxicity of CNTs, while not able to be quantified, did not hinder growth enough to prevent the cells from surviving for two weeks. This can be confirmed by immunofluorescence staining showing, viable cells with stained nuclei, and successful expression of α-actinin and Cx43 throughout all three conditions. While there were changes in the protein expression between the two measured samples for each condition, no conclusions can be drawn from this data. However, if repeated, there is a strong possibility results demonstrating improvements in expression based off the known effects the increased mechanical and electrical properties would have on these cells.

7. Future Directions

As material technology advances, nanomaterials are being used more frequently to enhance natural biomaterials. Fibrin, collagen, silk, chitosan, gelatin, alginate, hyaluronic acid, and extracellular matrix have all been used to demonstrate improvement in cardiomyocyte cultures. In addition to carbon nanotubes, gold nanorods, and silicon nanowires all have advantages in the field of cardiac tissue engineering. To expand on this project, different biomaterials and nanomaterials can be selected to test in a side-by-side comparison using a three-phase experimental framework to evaluate the effects of combining natural biopolymer hydrogels with functional nanomaterials to improve cardiomyocyte maturation and performance.

First, standardizing mechanical, electrical, and biological assessments across a diverse combination of materials, a new study could reveal the cellular mechanisms driving cellular development in engineered heart tissue. Rheology, DMA, and electrophysiology experiments will highlight key differences in how the materials behave in comparison to one another.

Second, cellular response to the engineered constructs could then be evaluated with a two-tiered approach. Functional and morphological responses will be quantified through high-resolution confocal microscopy to assess sarcomere organization and cell alignment, calcium transient analysis to evaluate excitation–contraction coupling, and twitch force measurements to determine contractile strength and kinetics.

Third, in parallel, multi-omics profiling will enable assessment of nanomaterial-specific effects on cellular growth, proliferation and function. Transcriptomic profiling can be conducted using both bulk RNA sequencing (RNA-seq) and single-cell RNA sequencing (scRNA-seq) to capture gene expression dynamics at both the population and individual cell levels [90]. These high-throughput techniques enable comprehensive quantification of the transcriptome, identifying differentially expressed genes and potentially uncovering novel transcripts associated with specific biomaterial conditions [90].

Proteomics can provide information on global transcriptional changes, and global protein expression levels as the cell responds to conditional changes, environmental changes, and biomaterials [90]. Not only does this technique show how protein levels and locations are a function of a cell's environment, but due to proteins being pleiotropic in nature, respond to dynamic protein-protein interactions [90]. Unlike transcriptomics, which infers protein expression from RNA abundance, proteomics directly captures the functional output of gene expression, including post-translational modifications and subcellular localization. This is particularly important in cardiac cells, where protein–protein interactions and complex signaling networks play critical roles in mechanosensing and excitation–contraction coupling [90]. Using LC-MS/MS, proteomics can reveal proteins that are differently expressed in response to biomaterials, which processes they are involved in, i.e metabolism, cytoskeleton organization, apoptosis [90].

Metabolomics identifies and quantifies small molecules resulting from the breakdown of food, drugs, chemicals, and are a direct result of the enzymatic activity in a cell [90]. This gives information about cell phenotypes and developmental stages. Nuclear magnetic resonance (NMR) is an in-depth analysis of metabolites and allows for mapping metabolite function within signaling pathways contributing to understanding of biological mechanisms. This technique can be crucial for a deeper understanding of nanomaterial and toxicity [90]. For example, a study screening liver and serum metabolites in mice revealed that higher doses of SiO2 correlated with a depletion of free fatty acids in lipid metabolism [90].

The integration of these omics' platforms would enable the identification of key signaling pathways, regulatory networks, and metabolic shifts associated with material–cell interactions. Altogether, this three-phase approach of 1) hydrogel mechanical and electrical characterization, 2) cell culture functional studies, and 3) multi-omics studies, could systematically test different combinations of natural biopolymer hydrogel scaffolds and nanomaterials. With repeatable hydrogel and cell culture characterization data, downstream analysis could elucidate the underlying biological mechanisms on how cardiomyocytes respond to different nanomaterials. Ultimately, moving the field towards a solution to repairing a damaged myocardium and contribute to the development of effective therapies for myocardial regeneration.

References

1. Di Cesare, Mariachiara, et al. “The Heart of the World.” *Global Heart*, vol. 19, no. 1, 2024, pp. 11–11, https://doi.org/10.5334/gh.1288.
2. “Decline in Deaths from Heart Disease and Stroke — United States, 1900–1999.” *MMWR. Morbidity and Mortality Weekly Report*, vol. 48, no. 30, 1999, pp. 649–56.
3. Litviňuková, Monika, et al. “Cells of the Adult Human Heart.” *Nature*, vol. 588, no. 7838, 2020, pp. 466–72, https://doi.org/10.1038/s41586-020-2797-4.
4. El-Husseiny, Hussein M., et al. “Stimuli-Responsive Hydrogels: Smart State of-the-Art Platforms for Cardiac Tissue Engineering.” *Frontiers in Bioengineering and Biotechnology*, vol. 11, 2023, pp. 1174075–1174075, https://doi.org/10.3389/fbioe.2023.1174075.
5. Parviz, Yasir, et al. “Cellular and Molecular Approaches to Enhance Myocardial Recovery after Myocardial Infarction.” *Cardiovascular Revascularization Medicine*, vol. 20, no. 4, 2019, pp. 351–64, https://doi.org/10.1016/j.carrev.2018.05.021.
6. Yu, Xuejing. “Application of Hydrogels in Cardiac Regeneration.” *Cardiology and Therapy*, vol. 12, no. 4, 2023, pp. 637–74, https://doi.org/10.1007/s40119-023-00339-0.
7. Hinderer, Svenja, and Katja Schenke-Layland. “Cardiac Fibrosis – A Short Review of Causes and Therapeutic Strategies.” *Advanced Drug Delivery Reviews*, vol. 146, 2019, pp. 77–82, https://doi.org/10.1016/j.addr.2019.05.011.
8. Nguyen, Anh H., et al. “Cardiac Tissue Engineering: State-of-the-Art Methods and Outlook.” *Journal of Biological Engineering*, vol. 13, no. 1, 2019, pp. 57–21, https://doi.org/10.1186/s13036-019-0185-0.
9. Pezhouman, Arash, et al. “Cardiac Regeneration – Past Advancements, Current Challenges, and Future Directions.” *Journal of Molecular and Cellular Cardiology*, vol. 182, 2023, pp. 75–85, https://doi.org/10.1016/j.yjmcc.2023.07.009.
10. Elkhoury, Kamil, et al. “Biofabrication of Natural Hydrogels for Cardiac, Neural, and Bone Tissue Engineering Applications.” *Bioactive Materials*, vol. 6, no. 11, 2021, pp. 3904–23, https://doi.org/10.1016/j.bioactmat.2021.03.040.
11. Yu, Xuejing. “Application of Hydrogels in Cardiac Regeneration.” *Cardiology and Therapy*, vol. 12, no. 4, 2023, pp. 637–74, https://doi.org/10.1007/s40119-023-00339-0.
12. Stoppel, Whitney L., et al. “Electrical and Mechanical Stimulation of Cardiac Cells and Tissue Constructs.” *Advanced Drug Delivery Reviews*, vol. 96, 2016, pp. 135–55, https://doi.org/10.1016/j.addr.2015.07.009.
13. Shih, H. T. “Anatomy of the Action Potential in the Heart.” *Texas Heart Institute Journal*, vol. 21, no. 1, 1994, pp. 30–41.
14. Walker, C. Allyson, and Francis G. Spinale. “The Structure and Function of the Cardiac Myocyte: A Review of Fundamental Concepts.” *The Journal of Thoracic and Cardiovascular Surgery*, vol. 118, no. 2, 1999, pp. 375–82, https://doi.org/10.1016/S0022-5223(99)70233-3.
15. Szedlak, P., et al. “Cardiac Muscle Physiology.” *BJA Education*, vol. 23, no. 9, 2023, pp. 350–57, https://doi.org/10.1016/j.bjae.2023.05.004.
16. Niessen, Carien M., and Cara J. Gottardi. “Molecular Components of the Adherens Junction.” *Biochimica et Biophysica Acta. Biomembranes*, vol. 1778, no. 3, 2008, pp. 562–71, https://doi.org/10.1016/j.bbamem.2007.12.015.

17. Kowalczyk, Andrew P., and Kathleen J. Green. "Structure, Function, and Regulation of Desmosomes." *Progress in Molecular Biology and Translational Science*, vol. 116, Academic Press, 2013, pp. 95–118, https://doi.org/10.1016/B978-0-12-394311-8.00005-4.
18. "Gap Junctions: Structure and Function (Review)." *Molecular Membrane Biology*, 2002, https://doi.org/10.1080/09687680210139839.
19. Sequeira, Vasco, et al. "The Physiological Role of Cardiac Cytoskeleton and Its Alterations in Heart Failure." *Biochimica et Biophysica Acta. Biomembranes*, vol. 1838, no. 2, 2014, pp. 700–22, https://doi.org/10.1016/j.bbamem.2013.07.011.
20. Caporizzo, Matthew A., and Benjamin L. Prosser. "The Microtubule Cytoskeleton in Cardiac Mechanics and Heart Failure." *Nature Reviews Cardiology*, vol. 19, no. 6, 2022, pp. 364–78, https://doi.org/10.1038/s41569-022-00692-y.
21. Uchida, Keita, et al. "Cardiomyocyte Microtubules: Control of Mechanics, Transport, and Remodeling." *Annual Review of Physiology*, vol. 84, no. 1, 2022, pp. 257–83, https://doi.org/10.1146/annurev-physiol-062421-040656.
22. Karbassi, Elaheh, et al. "Cardiomyocyte Maturation: Advances in Knowledge and Implications for Regenerative Medicine." *Nature Reviews Cardiology*, vol. 17, no. 6, 2020, pp. 341–59, https://doi.org/10.1038/s41569-019-0331-x.
23. Parish, David C., et al. "Mechanism of Death: There's More to It than Sudden Cardiac Arrest." *Journal of Thoracic Disease*, vol. 10, no. 5, 2018, pp. 3081–87, https://doi.org/10.21037/jtd.2018.04.113.
24. Kolwicz, Stephen C., et al. "Cardiac Metabolism and Its Interactions with Contraction, Growth, and Survival of the Cardiomyocte." *Circulation Research*, vol. 113, no. 5, 2013, https://doi.org/10.1161/CIRCRESAHA.113.302095.
25. Doenst, Torsten, et al. "Cardiac Metabolism in Heart Failure: Implications Beyond ATP Production." *Circulation Research*, vol. 113, no. 6, 2013, pp. 709–24, https://doi.org/10.1161/CIRCRESAHA.113.300376.
26. Gabriel-Costa, Daniele. "The Pathophysiology of Myocardial Infarction-Induced Heart Failure." *Pathophysiology (Amsterdam)*, vol. 25, no. 4, 2018, pp. 277–84, https://doi.org/10.1016/j.pathophys.2018.04.003.
27. Basso, C., and G. Thiene. "The Pathophysiology of Myocardial Reperfusion: A Pathologist's Perspective." *Heart (British Cardiac Society)*, vol. 92, no. 11, 2006, pp. 1559–62, https://doi.org/10.1136/hrt.2005.086959.
28. Azevedo, Paula S., et al. "Cardiac Remodeling: Concepts, Clinical Impact, Pathophysiological Mechanisms and Pharmacologic Treatment." *Arquivos Brasileiros de Cardiologia*, vol. 106, no. 1, 2016, pp. 62–69, https://doi.org/10.5935/abc.20160005.
29. Schirone, Leonardo, et al. "An Overview of the Molecular Mechanisms Associated with Myocardial Ischemic Injury: State of the Art and Translational Perspectives." *Cells (Basel, Switzerland)*, vol. 11, no. 7, 2022, pp. 1165-, https://doi.org/10.3390/cells11071165.
30. Hashmi, Satwat, and Suhail Al-Salam. "Acute Myocardial Infarction and Myocardial Ischemia-Reperfusion Injury: A Comparison." *International Journal of Clinical and Experimental Pathology*, vol. 8, no. 8, 2015, pp. 8786–96.
31. He, Jianfeng, et al. "Myocardial Ischemia/Reperfusion Injury: Mechanisms of Injury and Implications for Management (Review)." *Experimental and Therapeutic Medicine*, vol. 23, no. 6, 2022, https://doi.org/10.3892/etm.2022.11357.

32. Angelovski, Marija, et al. “Myocardial Infarction and Oxidative Damage in Animal Models: Objective and Expectations from the Application of Cysteine Derivatives.” *Toxicology Mechanisms and Methods*, vol. 33, no. 1, 2023, pp. 1–17, https://doi.org/10.1080/15376516.2022.2069530.
33. Yadid, Moran, et al. “Bioengineering Approaches to Treat the Failing Heart: From Cell Biology to 3D Printing.” *Nature Reviews Cardiology*, vol. 19, no. 2, 2022, pp. 83–99, https://doi.org/10.1038/s41569-021-00603-7.
34. Terashvili, Maia, and Zeljko J. Bosnjak. “Stem Cell Therapies in Cardiovascular Disease.” *Journal of Cardiothoracic and Vascular Anesthesia*, vol. 33, no. 1, 2019, pp. 209–22, https://doi.org/10.1053/j.jvca.2018.04.048.
35. Augustine, Robin, et al. “Stem Cell-Based Approaches in Cardiac Tissue Engineering: Controlling the Microenvironment for Autologous Cells.” *Biomedicine & Pharmacotherapy*, vol. 138, 2021, pp. 111425–111425, https://doi.org/10.1016/j.biopha.2021.111425.
36. Son, Yura, and Wuqiang Zhu. “Gene Therapy for Cardiomyocyte Renewal: Cell Cycle, a Potential Therapeutic Target.” *Molecular Diagnosis & Therapy*, vol. 27, no. 2, 2023, pp. 129–40, https://doi.org/10.1007/s40291-022-00625-y.
37. Yu, Xuejing. “Application of Hydrogels in Cardiac Regeneration.” *Cardiology and Therapy*, vol. 12, no. 4, 2023, pp. 637–74, https://doi.org/10.1007/s40119-023-00339-0.
38. Akbarzadeh, Aram, et al. “Whole-Heart Tissue Engineering and Cardiac Patches: Challenges and Promises.” *Bioengineering (Basel)*, vol. 10, no. 1, 2023, pp. 106-, https://doi.org/10.3390/bioengineering10010106.
39. Gil-Cabrerizo, Paula, et al. “Cardiac Tissue Engineering for Myocardial Infarction Treatment.” *European Journal of Pharmaceutical Sciences*, vol. 185, 2023, pp. 106439–106439, https://doi.org/10.1016/j.ejps.2023.106439.
40. Sanz-Horta, Raúl, et al. “Technological Advances in Fibrin for Tissue Engineering.” *Journal of Tissue Engineering*, vol. 14, 2023, pp. 20417314231190288–20417314231190288, https://doi.org/10.1177/20417314231190288.
41. Barsotti, Maria Chiara, et al. “Fibrin as a Scaffold for Cardiac Tissue Engineering.” *Biotechnology and Applied Biochemistry*, vol. 58, no. 5, 2011, pp. 301–10, https://doi.org/10.1002/bab.49.
42. Zuo, Xianghao, et al. “Engineering Collagen-Based Biomaterials for Cardiovascular Medicine.” *Collagen and Leather*, vol. 6, no. 1, 2024, pp. 1–23, https://doi.org/10.1186/s42825-024-00174-6.
43. Abraham, Leah C., et al. “Guide to Collagen Characterization for Biomaterial Studies.” *Journal of Biomedical Materials Research. Part B, Applied Biomaterials*, vol. 87B, no. 1, 2008, pp. 264–85, https://doi.org/10.1002/jbm.b.31078.
44. Badii, Farah, and Nazlin K. Howell. “Elucidation of the Effect of Formaldehyde and Lipids on Frozen Stored Cod Collagen by FT-Raman Spectroscopy and Differential Scanning Calorimetry.” *Journal of Agricultural and Food Chemistry*, vol. 51, no. 5, 2003, pp. 1440–46, https://doi.org/10.1021/jf020492u.
45. Coradin, Thibaud, et al. “Type I Collagen-Fibrin Mixed Hydrogels: Preparation, Properties and Biomedical Applications.” *Gels*, vol. 6, no. 4, 2020, pp. 36-, https://doi.org/10.3390/gels6040036.

46. Ye, Kathy Yuan, et al. “Encapsulation of Cardiomyocytes in a Fibrin Hydrogel for Cardiac Tissue Engineering.” *Journal of Visualized Experiments*, no. 55, 2011, https://doi.org/10.3791/3251.
47. Kaiser, Nicholas J., et al. “Optimizing Blended Collagen-Fibrin Hydrogels for Cardiac Tissue Engineering with Human iPSC-Derived Cardiomyocytes.” *ACS Biomaterials Science & Engineering*, vol. 5, no. 2, 2019, pp. 887–99, https://doi.org/10.1021/acsbiomaterials.8b01112.
48. Edalat, Sam G., et al. “Collagen Type I Containing Hybrid Hydrogel Enhances Cardiomyocyte Maturation in a 3D Cardiac Model.” *Polymers*, vol. 11, no. 4, 2019, pp. 687-, https://doi.org/10.3390/polym11040687.
49. Kim, Oleg V., et al. “Structural Basis for the Nonlinear Mechanics of Fibrin Networks under Compression.” *Biomaterials*, vol. 35, no. 25, 2014, pp. 6739–49, https://doi.org/10.1016/j.biomaterials.2014.04.056.
50. Shapira-Schweitzer, Keren, and Dror Seliktar. “Matrix Stiffness Affects Spontaneous Contraction of Cardiomyocytes Cultured within a PEGylated Fibrinogen Biomaterial.” *Acta Biomaterialia*, vol. 3, no. 1, 2007, pp. 33–41, https://doi.org/10.1016/j.actbio.2006.09.003.
51. Israeli-Rosenberg, Sharon, et al. “Integrins and Integrin-Associated Proteins in the Cardiac Myocyte.” Circulation Research, vol. 114, no. 3, 2014, pp. 572–86, https://doi.org/10.1161/CIRCRESAHA.114.301275.
52. Peterson, Caroline M., et al. “Covalent Capture of a Collagen Mimetic Peptide with an Integrin-Binding Motif.” Biomacromolecules, vol. 23, no. 6, 2022, pp. 2396–403, https://doi.org/10.1021/acs.biomac.2c00155.
53. Jokinen, Johanna, et al. “Integrin-Mediated Cell Adhesion to Type I Collagen Fibrils.” The Journal of Biological Chemistry, vol. 279, no. 30, 2004, pp. 31956–63, https://doi.org/10.1074/jbc.M401409200.
54. Ashtari, Khadijeh, et al. “Electrically Conductive Nanomaterials for Cardiac Tissue Engineering.” *Advanced Drug Delivery Reviews*, vol. 144, 2019, pp. 162–79, https://doi.org/10.1016/j.addr.2019.06.001.
55. Shin, Su Ryon, et al. “Carbon-Nanotube-Embedded Hydrogel Sheets for Engineering Cardiac Constructs and Bioactuators.” *ACS Nano*, vol. 7, no. 3, 2013, pp. 2369–80, https://doi.org/10.1021/nn305559j.
56. Yu, Hongsheng, et al. “Mechanically and Electrically Enhanced CNT–Collagen Hydrogels As Potential Scaffolds for Engineered Cardiac Constructs.” *ACS Biomaterials Science & Engineering*, vol. 3, no. 11, 2017, pp. 3017–21, https://doi.org/10.1021/acsbiomaterials.6b00620.
57. Mim, Juhi Jannat, et al. “A Comprehensive Review on the Biomedical Frontiers of Nanowire Applications.” *Heliyon*, vol. 10, no. 8, 2024, pp. e29244-, https://doi.org/10.1016/j.heliyon.2024.e29244.
58. Mim, Juhi Jannat, et al. “A Comprehensive Review on the Biomedical Frontiers of Nanowire Applications.” *Heliyon*, vol. 10, no. 8, 2024, pp. e29244-, https://doi.org/10.1016/j.heliyon.2024.e29244.

59. Liu, Haitao, et al. *Nanobiotechnology: 1D Nanomaterial Building Blocks for Cellular Interfaces and Hybrid Tissues.* Tufts University. Tisch Library., 2018.
60. Puglisi, Rosaria A., et al. "Chemical Vapor Deposition Growth of Silicon Nanowires with Diameter Smaller Than 5 Nm." *ACS Omega*, vol. 4, no. 19, 2019, pp. 17967–71, https://doi.org/10.1021/acsomega.9b01488.
61. Tan, Yu, et al. "Silicon Nanowire-Induced Maturation of Cardiomyocytes Derived from Human Induced Pluripotent Stem Cells." *Nano Letters*, vol. 15, no. 5, 2015, pp. 2765–72, https://doi.org/10.1021/nl502227a.
62. Li, Chia-Chen, et al. "A New and Acid-Exclusive Method for Dispersing Carbon Multi-Walled Nanotubes in Aqueous Suspensions." *Colloids and Surfaces. A, Physicochemical and Engineering Aspects*, vol. 297, no. 1, 2007, pp. 275 https://doi.org/10.1016/j.colsurfa.2006.10.022.
63. "Spectroscopic Investigation of Modified Single Wall Carbon Nanotube (SWCNT)." *Journal of Modern Physics*, https://doi.org/10.4236/jmp.2011.26063.
64. Gerasimenko, Alexander Yu, et al. "The Study of the Interaction Mechanism between Bovine Serum Albumin and Single-Walled Carbon Nanotubes Depending on Their Diameter and Concentration in Solid Nanocomposites by Vibrational Spectroscopy." *Spectrochimica Acta. Part A, Molecular and Biomolecular Spectroscopy*, vol. 227, 2020, pp. 117682-, https://doi.org/10.1016/j.saa.2019.117682.
65. Kalluri, Ankarao, et al. "Exfoliated and Water Dispersible Biocarbon Nanotubes for Enzymology Applications." *Methods in Enzymology*, vol. 630, 2020, pp. 407-, https://doi.org/10.1016/bs.mie.2019.11.010.
66. 55) "Application of Bile Acids for Biomedical Devices and Sensors." *Medical Devices & Sensors*, https://doi.org/10.1002/mds3.10119.
67. Lin, Shangchao, and Daniel Blankschtein. "Role of the Bile Salt Surfactant Sodium Cholate in Enhancing the Aqueous Dispersion Stability of Single-Walled Carbon Nanotubes: A Molecular Dynamics Simulation Study." *The Journal of Physical Chemistry. B*, vol. 114, no. 47, 2010, pp. 15616–25, https://doi.org/10.1021/jp1076406.
68. Jiang, Xinrong, et al. "Understanding the Influence of Single-Walled Carbon Nanotube Dispersion States on the Microstructure and Mechanical Properties of Wet-Spun Fibers." *Carbon (New York)*, vol. 169, 2020, pp. 17–24, https://doi.org/10.1016/j.carbon.2020.05.080.
69. Gubitosi, Marta, et al. "Characterization of Carbon Nanotube Dispersions in Solutions of Bile Salts and Derivatives Containing Aromatic Substituents." *The Journal of Physical Chemistry. B*, vol. 118, no. 4, 2014, pp. 1012–21, https://doi.org/10.1021/jp407145t.
70. Attal, S., et al. "Determination of the Concentration of Single-Walled Carbon Nanotubes in Aqueous Dispersions Using UV−Visible Absorption Spectroscopy." *Analytical Chemistry (Washington)*, vol. 78, no. 23, 2006, pp. 8098–104, https://doi.org/10.1021/ac060990s.
71. Farkas, Natalia, and John A. Kramar. "Dynamic Light Scattering Distributions by Any Means." *Journal of Nanoparticle Research : An Interdisciplinary Forum for Nanoscale Science and Technology*, vol. 23, no. 5, 2021, https://doi.org/10.1007/s11051-021-05220-6.

72. Jia, Zixian, et al. “Dynamic Light Scattering: A Powerful Tool for In Situ Nanoparticle Sizing.” *Colloids and Interfaces*, vol. 7, no. 1, 2023, pp. 15-, https://doi.org/10.3390/colloids7010015.
73. White, Brian, et al. “Zeta-Potential Measurements of Surfactant-Wrapped Individual Single-Walled Carbon Nanotubes.” Journal of Physical Chemistry. C, vol. 111, no. 37, 2007, pp. 13684–90, https://doi.org/10.1021/jp070853e.
74. Kumar, Pradip, and H. B. Bohidar. “Aqueous Dispersion Stability of Multi-Carbon Nanoparticles in Anionic, Cationic, Neutral, Bile Salt and Pulmonary Surfactant Solutions.” Colloids and Surfaces. A, Physicochemical and Engineering Aspects, vol. 361, no. 1, 2010, pp. 13–24, https://doi.org/10.1016/j.colsurfa.2010.03.009.
75. Gerasimenko, Alexander Yu, et al. “The Study of the Interaction Mechanism between Bovine Serum Albumin and Single-Walled Carbon Nanotubes Depending on Their Diameter and Concentration in Solid Nanocomposites by Vibrational Spectroscopy.” *Spectrochimica Acta. Part A, Molecular and Biomolecular Spectroscopy*, vol. 227, 2020, pp. 117682-, https://doi.org/10.1016/j.saa.2019.117682.
76. Kalluri, Ankarao, et al. “Exfoliated and Water Dispersible Biocarbon Nanotubes for Enzymology Applications.” *Methods in Enzymology*, vol. 630, 2020, pp. 407-, https://doi.org/10.1016/bs.mie.2019.11.010.
77. Du, Peng, et al. “Adsorption of Bovine Serum Albumin and Lysozyme on Functionalized Carbon Nanotubes.” *Journal of Physical Chemistry. C*, vol. 118, no. 38, 2014, pp. 22249–57, https://doi.org/10.1021/jp5044943.
78. “Application of Bile Acids for Biomedical Devices and Sensors.” *Medical Devices & Sensors*, https://doi.org/10.1002/mds3.10119.
79. Li, Lili, et al. “Interaction of Carboxylated Single-Walled Carbon Nanotubes with Bovine Serum Albumin.” *Spectrochimica Acta. Part A, Molecular and Biomolecular Spectroscopy*, vol. 105, 2013, pp. 45–51, https://doi.org/10.1016/j.saa.2012.11.111.
80. Zuidema, Jonathan M., et al. “A Protocol for Rheological Characterization of Hydrogels for Tissue Engineering Strategies.” *Journal of Biomedical Materials Research. Part B, Applied Biomaterials*, vol. 102, no. 5, 2014, pp. 1063–73, https://doi.org/10.1002/jbm.b.33088.
81. *Encapsulation of Cardiomyocytes in a Fibrin Hydrogel for Cardiac Tissue Engineering*. MyJoVE Corp.
82. Zuidema, Jonathan M., et al. “A Protocol for Rheological Characterization of Hydrogels for Tissue Engineering Strategies.” *Journal of Biomedical Materials Research. Part B, Applied Biomaterials*, vol. 102, no. 5, 2014, pp. 1063–73, https://doi.org/10.1002/jbm.b.33088.
83. Zuidema, Jonathan M., et al. “A Protocol for Rheological Characterization of Hydrogels for Tissue Engineering Strategies.” *Journal of Biomedical Materials Research. Part B, Applied Biomaterials*, vol. 102, no. 5, 2014, pp. 1063–73, https://doi.org/10.1002/jbm.b.33088.
84. Guillet, Jean-François, et al. “Electrical Properties of Double-Wall Carbon Nanotubes Nanocomposite Hydrogels.” Carbon (New York), vol. 146, 2019, pp. 542–48, https://doi.org/10.1016/j.carbon.2019.01.090.
85. Guo, Yuxuan, and William T. Pu. “Cardiomyocyte Maturation: New Phase in Development.” *Circulation Research*, vol. 126, no. 8, 2020, pp. 1086–106, https://doi.org/10.1161/CIRCRESAHA.119.315862.

86. Amezcua, Rodolfo, et al. “Nanomaterials for Cardiac Myocyte Tissue Engineering.” *Nanomaterials (Basel, Switzerland)*, vol. 6, no. 7, 2016, pp. 133-, https://doi.org/10.3390/nano6070133.
87. Scott, Louie, et al. “Carbon Nanotube-Based Scaffolds for Cardiac Tissue Engineering—Systematic Review and Narrative Synthesis.” *Bioengineering (Basel)*, vol. 8, no. 6, 2021, pp. 80-, https://doi.org/10.3390/bioengineering8060080.
88. Martinelli, Valentina, et al. “Improving Cardiac Myocytes Performance by Carbon Nanotubes Platforms.” *Frontiers in Physiology*, vol. 4, 2013, pp. 239–239, https://doi.org/10.3389/fphys.2013.00239.
89. Thompson, Brianna C., et al. “Carbon Nanotube Biogels.” *Carbon (New York)*, vol. 47, no. 5, 2009, pp. 1282–91, https://doi.org/10.1016/j.carbon.2009.01.013.
90. Kougkolos, Georgios, et al. “Hydrogels with Electrically Conductive Nanomaterials for Biomedical Applications.” *Journal of Materials Chemistry. B, Materials for Biology and Medicine*, vol. 11, no. 1, 2023, pp. 236–62, https://doi.org/10.1039/d2tb02019j.
91. “Optimizing a Spontaneously Contracting Heart Tissue Patch with Rat Neonatal Cardiac Cells on Fibrin Gel.” Journal of Tissue Engineering and Regenerative Medicine, 2017, https://doi.org/10.1002/term.1895.